nature energy

ARTICLES

https://doi.org/10.1038/s41560-021-00792-y

Check for updates

Ultra-high-voltage Ni-rich layered cathodes in practical Li metal batteries enabled by a sulfonamide-based electrolyte

Weijiang Xue[1], Mingjun Huang[2], Yutao Li[3], Yun Guang Zhu[4], Rui Gao[1], Xianghui Xiao[5], Wenxu Zhang[2], Sipei Li[4], Guiyin Xu[1], Yang Yu[6], Peng Li[1], Jeffrey Lopez[4], Daiwei Yu[7], Yanhao Dong[1]✉, Weiwei Fan[1], Zhe Shi[6], Rui Xiong[1,8], Cheng-Jun Sun[9], Inhui Hwang[9], Wah-Keat Lee[5], Yang Shao-Horn[4,6,10]✉, Jeremiah A. Johnson[2]✉ and Ju Li[1,6]✉

By increasing the charging voltage, a cell specific energy of >400 W h kg^{-1} is achievable with $LiNi_{0.8}Mn_{0.1}Co_{0.1}O_2$ in Li metal batteries. However, stable cycling of high-nickel cathodes at ultra-high voltages is extremely challenging. Here we report that a rationally designed sulfonamide-based electrolyte enables stable cycling of commercial $LiNi_{0.8}Co_{0.1}Mn_{0.1}O_2$ with a cut-off voltage up to 4.7 V in Li metal batteries. In contrast to commercial carbonate electrolytes, the electrolyte not only suppresses side reactions, stress-corrosion cracking, transition-metal dissolution and impedance growth on the cathode side, but also enables highly reversible Li metal stripping and plating leading to a compact morphology and low pulverization. Our lithium-metal battery delivers a specific capacity >230 mA h g^{-1} and an average Coulombic efficiency >99.65% over 100 cycles. Even under harsh testing conditions, the 4.7 V lithium-metal battery can retain >88% capacity for 90 cycles, advancing practical lithium-metal batteries.

There is an urgent demand for high-energy-density batteries[1,2] for portable electronic devices, drones and electric vehicles. While state-of-the-art lithium-ion batteries with graphite anodes have a cell-level[3,4] gravimetric energy density (E_g) of ~250 W h kg^{-1}, a much higher E_g of >400 W h kg^{-1} is in principle possible for lithium-metal batteries (LMBs) with high-energy-density cathodes such as nickel-rich $LiNi_xMn_yCo_{1-x-y}O_2$ (NMC)[5,6] and lithium metal anodes (LMAs). Achieving this goal requires great efforts in battery design and optimization, with elevated charging voltage and minimized excess components[3,7,8] (for example, LMAs and electrolyte), pushing all materials and cell parameters to their limits.

On the cathode side, elevating the upper cut-off voltage[1] is a straightforward way to increase the discharge capacity and energy density[9]. For example, an additional ~15–35% capacity could be gained by increasing the upper cut-off voltage of NMC cathodes from the traditional 4.3 V to 4.7 V (versus Li$^+$/Li)[10]. Unfortunately, this approach tends to induce instabilities in the bulk and at the surface of the cathode and thus significantly degrades cycle life. Such degradations become more serious[6,11] with increasing Ni content and higher cut-off voltage, especially for $LiNi_{0.8}Co_{0.1}Mn_{0.1}O_2$ (NMC811) of commercial interest. On the anode side, high reversibility[12,13] is essential to reduce the usage of excess lithium metal and electrolyte relative to the cathode. Finally, LMBs need to operate under practical conditions where a high-loading cathode (typical industry level is >3.5 mA h cm^{-2}), low negative to positive (N/P) ratio[13] and lean electrolyte (typical industry level for electrolyte to capacity (E/C) ratio is ~2–5 g (Ah)$^{-1}$) are required at the same time. These harsh conditions make it extremely difficult to maintain a satisfactory cycle life.

Many cathode degradation mechanisms are intensified in LMBs operated under high cut-off voltages (Fig. 1a,b), including cathode–electrolyte side reactions[14–16], bulk and surface phase transformation[17], cracking of the NMC secondary particles[17,18], over-growth of cathode–electrolyte interphases (CEIs), gas evolution[15] and transition metal (TM) dissolution[19]. Moreover, dissolved TMs eventually waft to the anode side where they can be reduced and accumulated, similar to the 'shuttling effect'[20,21] in lithium–sulfur batteries, leading to the destruction of the anode's solid–electrolyte interphase (SEI), consumption of active Li, and impedance growth. Also, failures[3,7,8] often occur on the LMA as the electrolyte influences the cycling morphology and reversibility of the LMA[22]. A limited cyclable Li inventory can be easily depleted by side reactions or become kinetically unreachable due to electronic/ionic isolation[23]. Lean electrolyte itself can also be rapidly depleted or contaminated by side reactions[24], and loss of ionic percolation can happen due to wetting of large-surface-area and large-thickness Li deposits.

Since the aforementioned challenges in high-voltage LMBs are closely related to the electrolyte, the design of novel liquid electrolytes, which have the desired compatibility with both high-voltage cathodes and LMAs, offers a promising solution.

[1]Department of Nuclear Science and Engineering, Massachusetts Institute of Technology, Cambridge, MA, USA. [2]Department of Chemistry, Massachusetts Institute of Technology, Cambridge, MA, USA. [3]Materials Science and Engineering Program and Texas Materials Institute, University of Texas at Austin, Austin, TX, USA. [4]Research Laboratory of Electronics, Massachusetts Institute of Technology, Cambridge, MA, USA. [5]National Synchrotron Light Source II, Brookhaven National Laboratory, Upton, NY, USA. [6]Department of Materials Science and Engineering, Massachusetts Institute of Technology, Cambridge, MA, USA. [7]Department of Electrical Engineering and Computer Science, Massachusetts Institute of Technology, Cambridge, MA, USA. [8]National Engineering Laboratory for Electric Vehicles, School of Mechanical Engineering, Beijing Institute of Technology, Beijing, China. [9]Advanced Photon Source, Argonne National Laboratory, Lemont, IL, USA. [10]Department of Mechanical Engineering, Massachusetts Institute of Technology, Cambridge, MA, USA. ✉e-mail: dongyh@mit.edu; shaohorn@mit.edu; jaj2109@mit.edu; liju@mit.edu

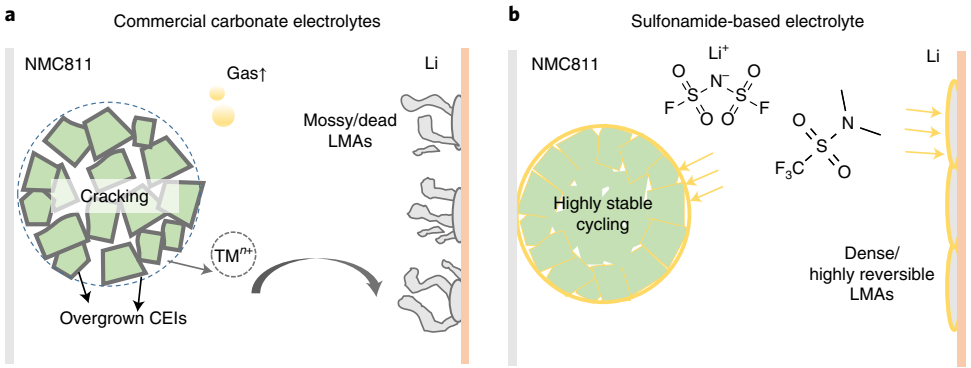

Fig. 1 | Challenges for durable high-voltage Li || NMC811 cells. a, With commercial carbonate electrolytes, severe side reactions between reactive NMC811 surfaces and electrolytes lead to serious gas evolution, TM dissolution, particle cracking and overgrown CEIs. Challenges in the LMA come from the formation of mossy/dead Li, severe side reactions and TM shuttling from the cathode side. **b**, Our sulfonamide-based electrolyte can suppress/delay particle cracking and mitigate cathode–electrolyte interfacial reactions, thus enabling a highly stable cathode. Our electrolyte also favours the formation of compact uniform Li and suppresses detrimental side reactions, thus enabling a highly reversible LMA.

High-concentration electrolytes[16,25,26], localized high-concentration electrolytes[8,27], 'full-fluorine electrolytes'[28,29], fluorinated ether-based electrolytes[30,31] and cyclic phosphate-based electrolytes[32] also show promise to enhance the cycling stability of Li || NMC batteries, yet the upper cut-off voltage reported to date is mostly limited to 4.5 V versus Li^+/Li. Moreover, it should be emphasized that the claimed improvements should be carefully evaluated under practical harsh conditions[7,8].

In the present work, we demonstrate a liquid electrolyte that enables stable ultra-high-voltage cycling (~4.7 V) of a high-nickel cathode (commercial NMC811) in practical LMBs (summary of prior work in Supplementary Table 1). In order to achieve compatibility with both high-voltage NMC811 and lithium metal, we selected the liquid aprotic *N*,*N*-dimethyltrifluoromethane-sulfonamide (DMTMSA) as the electrolyte solvent[33,34], which belongs to the sulfonamide family. A regular concentration (1 m, where m stands for molality) of LiFSI with DMTMSA (referred to as 1 m LiFSI/DMTMSA hereafter) enables highly reversible LMAs by favouring compact Li metal deposition morphologies and minimizing pulverization. It also enables stable cycling of NMC811 cathodes under 4.7 V with a high specific capacity of >230 mA h g^{-1} and an average Coulombic efficiency (CE) of >99.65% over 100 cycles, by suppressing cathode particle intergranular stress corrosion cracking (SCC), partially due to decreased TM ion solubility in the sulfonamide-based electrolyte. Together with cathode optimizations[35,36], this work points towards achieving durable ultra-high-voltage Ni-rich cathodes in practical LMBs.

The 1 m LiFSI/DMTMSA enables stable cycling of 4.7 V NMC811

Our 1 m LiFSI/DMTMSA electrolyte shows good Li^+ conductivity (Supplementary Table 2), good oxidation stability, compatibilities with high-voltage cathodes and the LMA and other benefits including good resistance to residual water and good wettability with separator (Supplementary Fig. 1 and Table 3). The cycling stability of 4.7 V NMC811 was tested with our 1 m LiFSI/DMTMSA electrolyte. A commercial carbonate electrolyte—1 M lithium hexafluorophosphate in ethylene carbonate and ethyl methyl carbonate (3:7 by weight) with 2 wt% vinylene carbonate (abbreviated as 1 M $LiPF_6$/EC-EMC + 2% VC hereafter, where M stands for molarity)—was used as the reference electrolyte.

To exclude the effect from LMA and investigate the 'intrinsic' cathode performance (Supplementary Fig. 2), a 'super-excessive condition' (thick Li metal, ~350 µm, and abundant electrolyte, ~80 µl) was used with the reference electrolyte (blue curves in Fig. 2a), which showed 76.1% capacity retention after 100 cycles at 0.5 C and low CEs of ~98% at the end of the cycling. In contrast, our 1 m LiFSI/DMTMSA electrolyte delivered a high discharge capacity of 231 mA h g^{-1} at 0.1 C, superior capacity retention of 88.1% after 100 cycles at 0.5 C and a high average CE of >99.65% (red curves in Fig. 2a) even under a 'stringent condition' (thin Li foil, ~60 µm, and limited electrolyte, ~20 µl), for which the reference electrolyte failed rapidly (Supplementary Fig. 2a). Despite the harsher testing conditions, our electrolyte showed less voltage decay (Fig. 2b), higher energy efficiency (Fig. 2c), higher first-cycle CE (Supplementary Fig. 3a) and more-stable voltage profiles (Fig. 2e) compared to the reference electrolyte (Fig. 2a–d and Supplementary Fig. 3b). An impressive average energy efficiency of ~97% (over 100 cycles)—a key factor for battery charging cost[37]—can also be achieved in 4.7 V NMC811, readily surpassing the target energy efficiency of 90–95% for next-generation high-voltage NMC[1].

Our electrolyte also improves rate capability (Supplementary Fig. 3c), offering high capacities of 205 mA h g^{-1} at 1 C and 186 mA h g^{-1} at 2 C. Moreover, the 4.7 V LMBs with our electrolyte exhibit excellent CEs of >99% even when cycled at 55 °C, compared to CEs of ~92% for the reference electrolyte (Supplementary Fig. 4). Considering the high-voltage instability of VC[38], the Li || NMC811 cell with 1 M $LiPF_6$/EC-EMC without VC was tested, which showed more capacity loss upon cycling at 25 °C (Supplementary Fig. 5) than the one with VC. Nevertheless, the cycling performance of both carbonate electrolytes is far worse than that of our 1 m LiFSI/DMTMSA electrolyte. Lastly, the superior cycling performance of our electrolyte is again demonstrated when cycled with lower cut-off voltages of 4.3 V and 4.5 V (Supplementary Fig. 6).

To gain insights into the degradation mechanisms, we conducted galvanostatic intermittent titration technique measurements for the cells after the 1st and 100th cycles. It is noted that the overpotentials of the cathode cycled in our electrolyte were much smaller than the one cycled in the reference electrolyte (Fig. 2f). Moreover, we note that the open-circuit voltage profiles (dashed curves in Supplementary Fig. 7a,b; consisted of data points after each relaxation step) barely change for all the samples, which suggests that the degradation of 4.7 V NMC811 under these conditions has a kinetic origin, guiding us to carefully inspect side reactions at the cathode surface (forming a high-impedance surface phase and CEIs) as well as inside the secondary particles. Lastly, before turning to detailed analysis of the NMC cathode and LMA, we emphasize that Al corrosion is suppressed in our electrolyte (LiFSI is known to corrode an

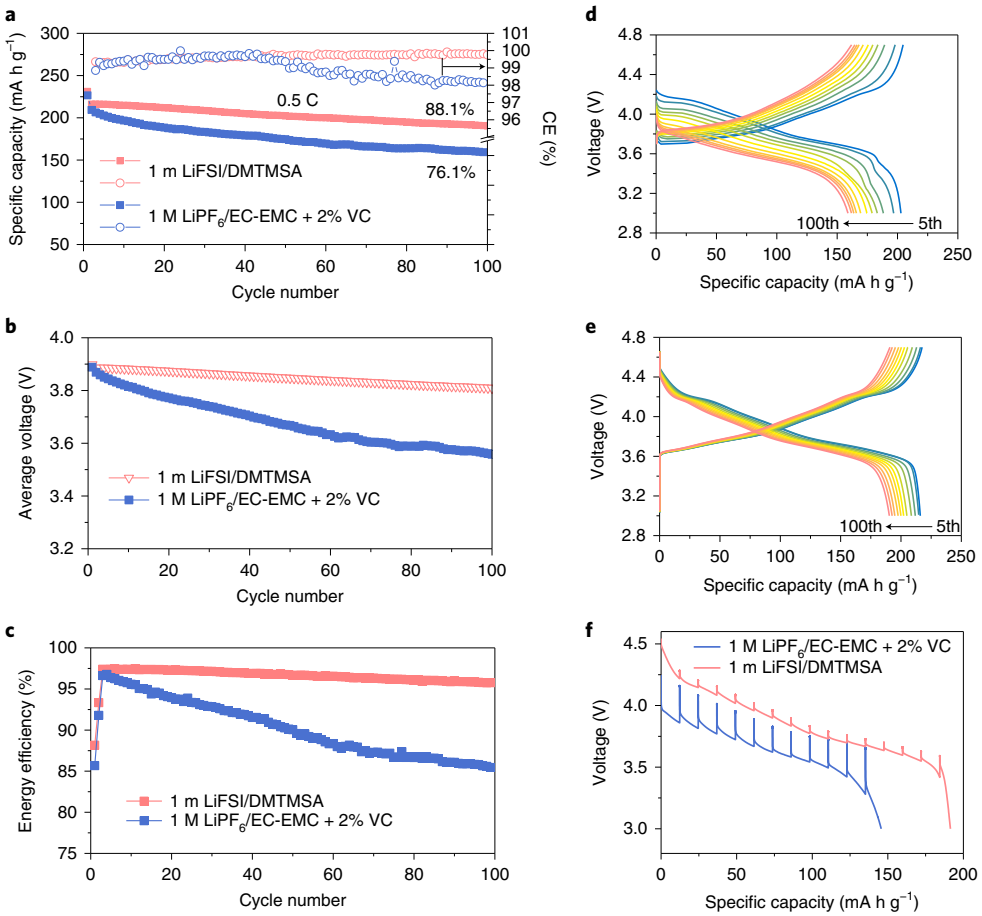

Fig. 2 | Electrochemical performances of Li || NMC811 cells using different electrolytes. a–c, Specific capacity and CE (**a**), average voltage (**b**) and energy efficiency (**c**) of the investigated electrolytes at 0.5 C (0.1 C for the first cycle). **d**,**e**, Corresponding voltage profiles of the cells using 1 M $LiPF_6$/EC-EMC + 2% VC (**d**) and 1 m LiFSI/DMTMSA (**e**) electrolytes. The curves in rainbow colours correspond to the voltage profiles from the 5th to 100th cycles. **f**, Discharge voltage profiles of galvanostatic intermittent titration technique measurements on the cells after 100 cycles. For cells with 1 m LiFSI/DMTMSA electrolyte, 'stringent conditions' (60 μm Li foil and 20 μl electrolyte) were used. For cells with 1 M $LiPF_6$/EC-EMC + 2% VC electrolyte, 'super-excessive conditions' (350 μm Li foil and 80 μl electrolyte) were used.

Al current collector, which limits its practical use) via the formation of an AlO_xF_y-like passivation layer (Supplementary Fig. 8) similar to that formed in $LiPF_6$-based electrolyte, which does not have the Al corrosion problem[39].

The 1 m LiFSI/DMTMSA suppresses cathode–electrolyte side reactions

To evaluate the side reactions between the NMC811 cathode and the electrolyte, we conducted accelerated degradation tests by continuously exposing the cathode to the most extreme electrochemical conditions at 4.7 V versus Li^+/Li. The 4.7 V float-test leakage current (Fig. 3a), which characterizes the side reaction rates, suggested that more side reactions happened for the cell cycled in the reference electrolyte than that cycled in our electrolyte (also confirmed by cathode surface morphologies in Supplementary Fig. 9). Compared to the reference electrolyte with a quasi-steady-state leakage current of ~17 μA, in ~5 h after an initial decay, the leakage current for our electrolyte monotonically decreased, reaching a minimum value of 3.2 μA at the end of a 20 h hold. This observation indicates a diminishing reaction rate and successfully passivated cathode surface.

The suppressed side reactions are further supported by much less CO_2 evolution (>~4.3 V) in our electrolyte (Fig. 3c) than in the reference one (Fig. 3d), measured by in situ differential electrochemical mass spectrometry (DEMS), without invoking other gas production (O_2, SO_2 and NO_2; Fig. 3c,d and Supplementary Fig. 10) up to 4.7 V versus Li^+/Li. Meanwhile, simultaneously suppressed TM dissolution is confirmed by inductively coupled plasma mass spectrometry (ICP-MS) measurements in Fig. 3b: after 100 cycles, an eightfold decrease in dissolved Ni and fourfold decrease in total TMs were achieved in our electrolyte with respect to the reference electrolyte.

To further characterize CEIs, X-ray photoelectron spectroscopy (XPS) measurements were conducted on the surface of the cathodes after the 100 cycles. Compared to the cathode cycled in the reference electrolyte (Fig. 3e,g), the one cycled in our electrolyte has a weaker C 1*s* signal (Fig. 3f, especially the peaks that can be attributed to C–O, C=O and poly(CO_3)) and stronger F 1*s* signal (Fig. 3h, especially the peak that can be attributed to F–Li). They indicate that the CEIs derived from our electrolyte should consist of more LiF-like inorganic components (which are known to be 'good' CEI components[12,26,29,30]) and less organic components (Supplementary Fig. 11). The XPS results also agree well with the time-of-flight secondary ion mass spectrometry (TOF-SIMS) measurements (Supplementary Fig. 12), where more LiF_2^- (representing inorganic components) and less C_2HO^- (representing organic components) fragments are detected for the cathode cycled with our electrolyte that the one with the reference electrolyte.

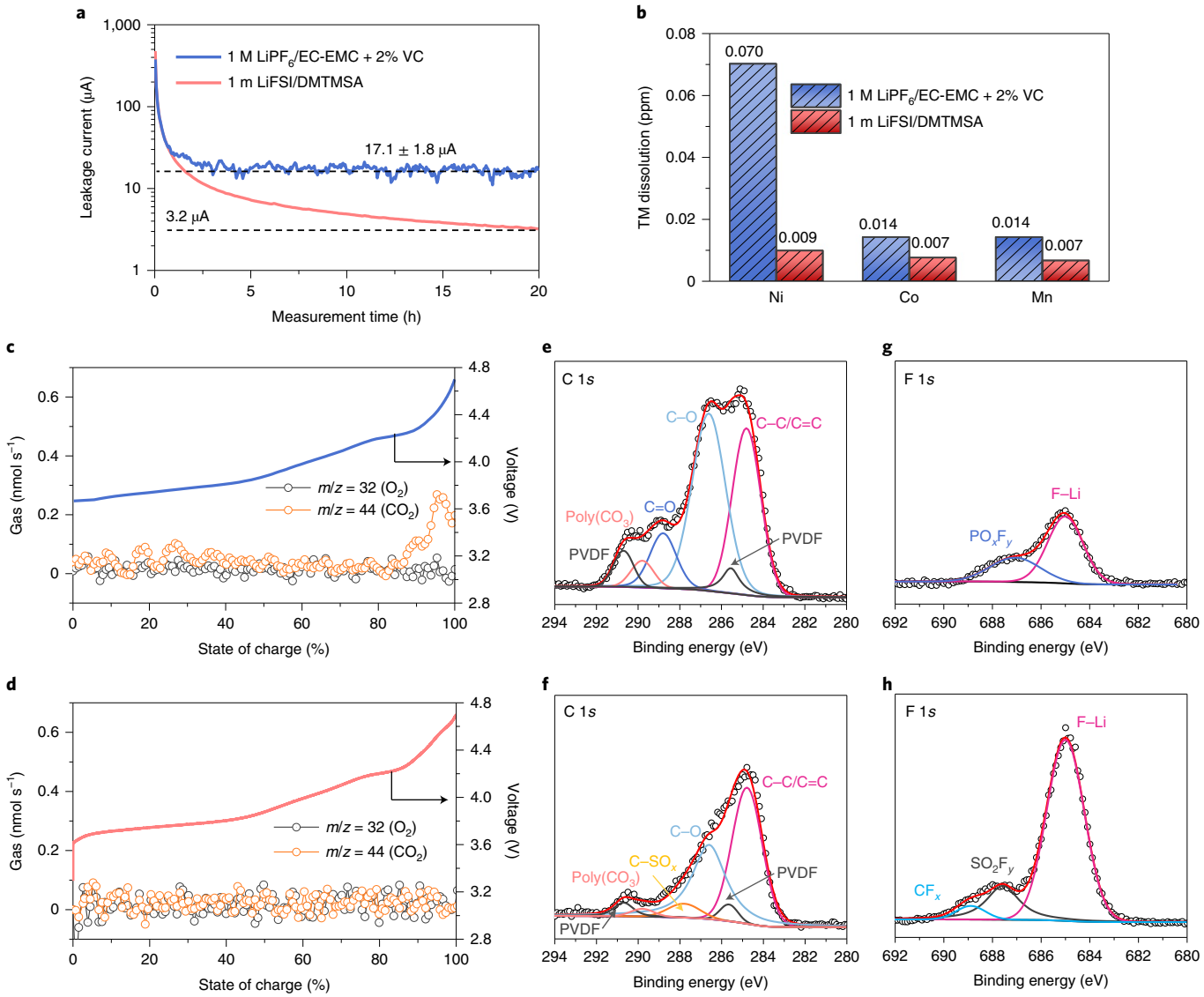

Fig. 3 | Characterizations of cathode–electrolyte side reactions and CEIs at 4.7 V cut-off voltage. a, Leakage currents during 4.7 V constant-voltage floating test of the NMC811 cathodes cycled in different electrolytes for 50 cycles. **b**, TM dissolution measured by ICP-MS after 100 cycles in different electrolytes. **c**,**d**, In situ DEMS analysis in half cells to monitor the gas evolution during first charging in 1 M $LiPF_6$/EC-EMC + 2% VC (**c**) and 1 m LiFSI/DMTMSA (**d**) electrolytes. Voltages profiles during charging are plotted as right *y* axis. **e**–**h**, XPS analysis for the NMC811 cathodes cycled in 1 M $LiPF_6$/EC-EMC + 2% VC (**e** and **f**) and 1 m LiFSI/DMTMSA (**g** and **h**) electrolytes for 100 cycles. PVDF, polyvinylidene fluoride. The black dots and red lines are original and fitted XPS spectra, respectively. The devolution spectra in different colours correspond to the labelled chemistries near the spectra.

The 1 m LiFSI/DMTMSA suppresses microstructural degradation

Intergranular cracking between connected primary particles in a secondary particle is a critical issue for the degradation of Ni-rich cathodes, especially with higher cut-off voltages and prolonged cycling[40,41], resulting in the loss of electrical contacts between primary particles. An increased electrochemical surface area also means more liquid electrolyte required for wetting (the liquid electrolyte in industry batteries, ~2–5 g $A^{-1}h^{-1}$, needs to wet the cathode, anode and separator, often making it the scarcest component), more side reactions and more electrolyte consumption. This phenomenon is apparently severe for the NMC811 cathodes cycled in the reference electrolyte, as the galvanostatic intermittent titration technique after cycling identified large overpotential growth in the form of ohmic loss (Supplementary Fig. 7) that is closely related to electron transport at the electrode level.

To characterize such microstructural degradation, cathodes after 100 cycles were cross-sectioned and inspected under scanning electron microscopy (SEM). While extensive cracking can be observed in the cathode cycled with the reference electrolyte (Fig. 4a,b), it is apparently suppressed or delayed with our electrolyte (Fig. 4c,d). More examples can be found in Supplementary Fig. 13. Note that complete elimination of the cracking is still challenging if ever possible, but it may not be a necessary condition to achieve a satisfactory cycling performance over a hundred cycles.) The morphology of cycled NMC811 secondary particles was next examined by three-dimensional tomography of the full-field X-ray imaging (FXI) at the National Synchrotron Light Source II (Brookhaven National Laboratory). The reconstructed images clearly contrast the cracking behaviour with the reference electrolyte (Fig. 4e, with severe cracking along radial direction) and our electrolyte (Fig. 4f, with intact primary particles).

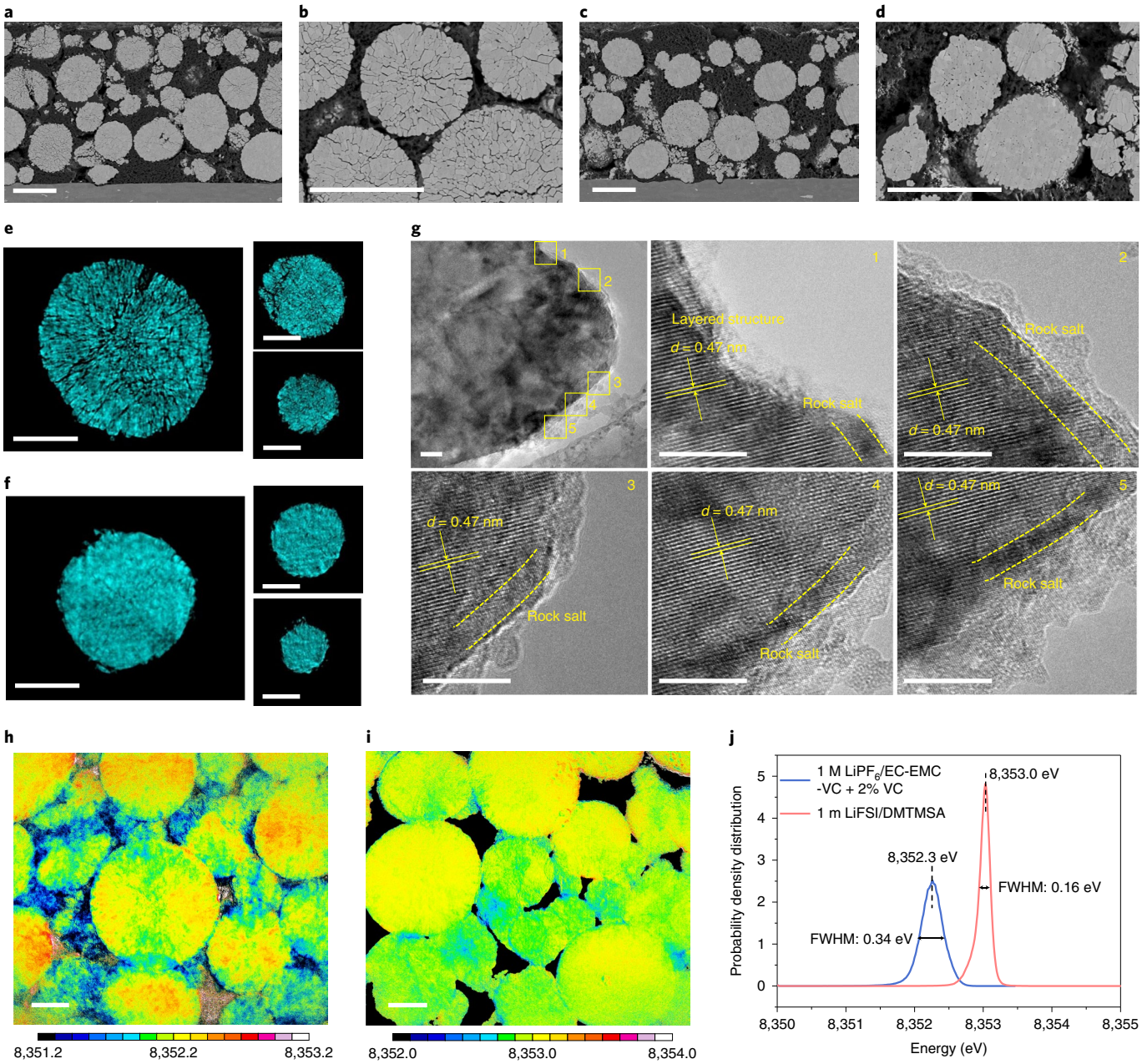

Fig. 4 | Structural characterizations of the cycled NMC811 cathodes with different electrolytes. a–d, SEM images of cross-sectioned NMC811 cathodes cycled in 1 M $LiPF_6$/EC-EMC + 2% VC (**a** and **b**) and 1 m LiFSI/DMTMSA (**c** and **d**) electrolytes. **e**,**f**, Two-dimensional cross-sections at different depths of the reconstructed three-dimensional tomography images of NMC particles cycled in 1 M $LiPF_6$/EC-EMC + 2% VC (**e**) and 1 m LiFSI/DMTMSA (**f**) electrolytes. **g**, High-resolution TEM images of NMC811 particles cycled in 1 m LiFSI/DMTMSA electrolyte. *d*, distance between lattice planes. **h**,**i**, Two-dimensional XANES mapping of NMC811 particles cycled in 1 M $LiPF_6$/EC-EMC + 2% VC (**h**) and 1 m LiFSI/DMTMSA (**i**) electrolytes for 100 cycles and then charged to 4.7 V versus Li^+/Li. The colour bars correspond to the white line peak position in eV. **j**, Statistical analysis of the whiteline distributions in particles in **h** and **i**. A smaller full width at half maximum (FWHM) in **j** represents less-scattered Ni oxidation states. Scale bars, 10 μm (**a–d**), 5 μm (**e**,**f**,**h**,**i**) and 10 nm (**g**).

The surface phase transition from a layered to resistive rock-salt NiO-like structure is known to degrade NMC cathode performance. Under high-resolution transmission electron microscopy (TEM), we found the transformed rack-salt layer is thin (~3–4 nm) and uniform (shown by panels 1–5 of Fig. 4g, taken from five local regions) over the surface of the cathode cycled in our electrolyte, while the one cycled with the reference electrolyte has a very thick rock-salt layer of >20 nm (Supplementary Fig. 14). This finding agrees well with the improved electrochemical performance by our electrolyte, especially the suppressed impedance growth in Fig. 2g. Since oxygen loss and cation densification are obviously involved in the layered-to-rock-salt surface phase transition, it is also consistent with the suppressed side reactions presented in Fig. 3.

The redox chemistry in bulk would be significantly affected by the loss of electrical contacts and phase transitions at cracking-exposed fresh surfaces. Using the X-ray absorption near-edge structure (XANES) mode of FXI, we mapped Ni oxidation states in the cycled cathodes at the fully charged state (that is, 4.7 V versus Li^+/Li). We

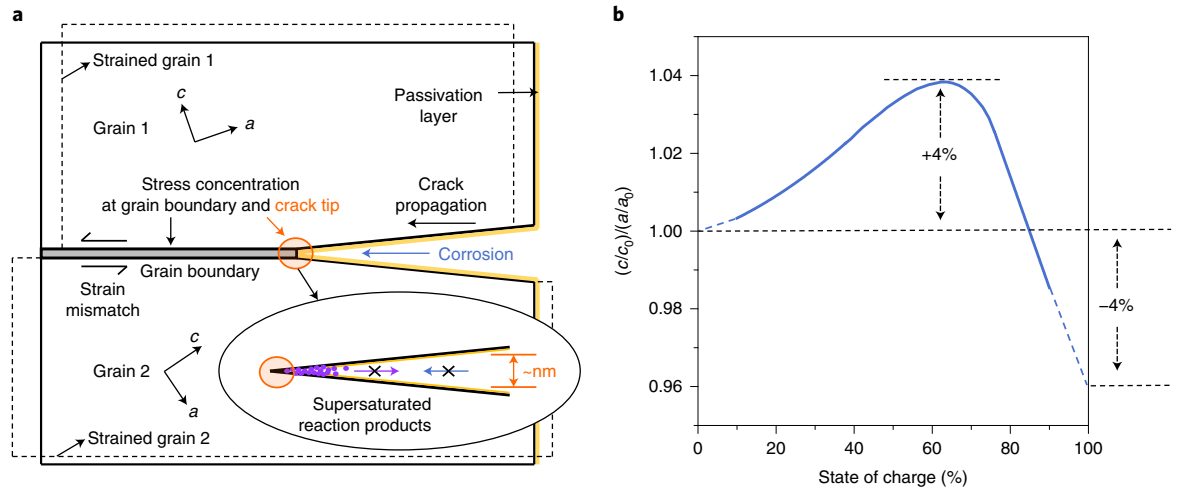

Fig. 5 | Proposed stress-corrosion cracking (SCC) mechanism for polycrystalline cathodes and its suppression by limiting reaction-product solubilities in the liquid electrolyte. a, Intergranular cracking beyond a purely mechanical event involves chemical interactions between the cathode grain boundary/surface region and electrolyte. SCC can be largely suppressed by our electrolyte, because it is less reactive and corrosive and the supersaturated side reaction products cannot diffuse away in the nano-channel near the crack tip. The dashed lines are schematics of the strained grains. **b**, The lattice anisotropy $(c/c_0)/(a/a_0)$ ratio as a function of state of charge in the NMC811 cathode[47]. The dashed lines are extrapolated data to fully charged and discharged states.

found that Ni has higher and more narrowly distributed oxidation states in the sample cycled in our electrolyte (Fig. 4h) than in the reference electrolyte (Fig. 4i). Here, the whiteline analysis was conducted on the signals collected from the particles that are not overlapping with each other (Supplementary Fig. 15). Therefore, the microstructural degradation, surface phase transition and bulk electrochemistry are apparently correlated, and all three issues have been successfully addressed by our electrolyte.

Previously, intergranular cracking was mostly attributed to mechanical stress created by anisotropic lattice expansion/shrinkage and heterogeneous charge/discharge kinetics during electrochemical cycling. However, in our work, cathodes with the same composition, microstructure, electrochemistry and testing conditions (except for the amount of electrolyte and LMA) showed large differences, and intergranular cracking can be suppressed with electrolytes even under deep-charge cycling at 4.7 V (electrolyte-modified cracking behaviour was also noted in the literature[42], albeit at lower cut-off voltages). In the literature, infused cathode coating[43,44] was also reported to relieve intergranular cracking in Ni-rich cathodes, which was explained by blocking the penetration of the electrolytes. This argument does not apply to our case, since we used the same NMC811 cathode. Therefore, our observation—a 'good' electrolyte can mitigate or slow down microstructure degradation of a deep-cycled Ni-rich cathode—demonstrates that the intergranular cracking should be more than a purely stress-driven event and the chemical interaction between the charged cathode grain boundary/surface region and electrolyte is also key. This is by definition a SCC process (Fig. 5a).

The proposed SCC mechanism is consistent with the observation that single-crystalline NMC (and $LiCoO_2$) with a similar size as the secondary particles of polycrystalline NMC does not crack as easily[45,46], indicating that uniform eigenstrain (that is, stress-free strain induced by lithiation/delithiation chemical expansion) does not crack the brittle ceramic particles despite its relatively large magnitude. It is the large linear-strain mismatch at grain boundaries[47]—given the ±4% change in anisotropic ratio $(c/c_0)/(a/a_0)$ during charge/discharge (Fig. 5b); here a_0 and c_0 denote the lattice parameters in fully discharged state, and a and c denote the lattice parameters during charge/discharge—that leads to either large elastic stress (~6 GPa with ~140 GPa Young's modulus[48]) or slippage (inelastic grain boundary sliding). Note the 6 GPa elastic stress does not even account for the concentration factor at the potential mode-II, mode-III or mixed-mode crack tip at grain boundary. The suppressed/delayed mode-I cracking in a 'good' electrolyte indicates that inelastic grain boundary slippage could relax stress build-up and cleavage. On the other hand, a 'bad' electrolyte can worsen the situation, where continuous side reactions corrode the cyclically slipping grain boundaries. Oxygen loss and TM dissolution into the electrolyte offer thermodynamic and kinetic advantage to the initiation and propagation of SCC and degrade the cathodes. The hypothetical SCC mechanism and its mitigation provide new insights into the intertwined electro-chemo-mechanics of oxide cathodes under extreme electrochemical conditions and synergize with recent progress in optimizing bulk electrode composition and crystallography[35,36].

Improved Li metal reversibility

Beyond the cathode, the cycling stability of LMBs also heavily relies on the compatibility between the electrolyte and LMA. Figure 6a shows the CEs evaluated by Li stripping/plating on Cu current collectors, where our 1 m LiFSI/DMTMSA electrolyte has an average CE of ~99% over 345 cycles, much higher than that of the reference electrolyte. The superior compatibility of our electrolyte was further demonstrated by the stable cycling of Li||Li symmetric cells in Fig. 6b, which shows much less polarization than the cells using the reference electrolyte. Moreover, our electrolyte enables remarkably stable cycling in an 'anode-free' cell consisting of a bare Cu current collector and high-loading NMC811 cathode with limited electrolyte (Supplementary Fig. 16). These results demonstrate excellent compatibility between our electrolyte and the LMA.

The Li metal morphology is critical to LMA reversibility. After long-term cycling, the thickness of LMA increases due to Li metal morphological instability, which contains SEIs, trapped gases[30] and liquid-infilled porosity. A less-compact, less-active layer, formed by dead Li, SEIs and high porosity, together with depleted Li inventory and liquid electrolyte (also contaminated), leads to impedance growth and premature cell failure on the anode side. It is also a safety risk in the event of accidents. This is the case for the LMA cycled in the reference electrolyte (Supplementary Fig. 17), where active Li was completely consumed, with a hugely swollen LMA,

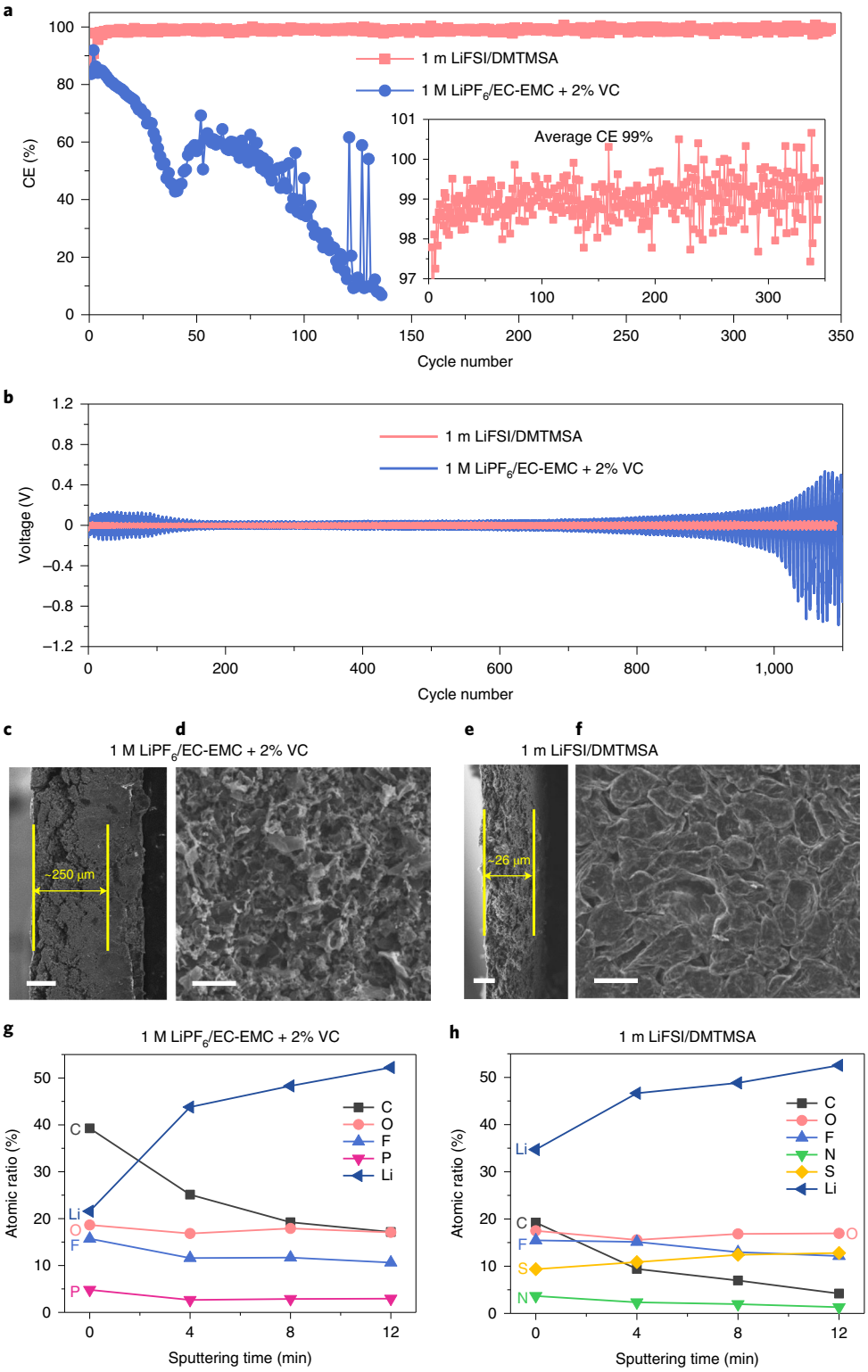

Fig. 6 | Electrochemical performance and characterizations of the LMA in different electrolytes. a, Li metal plating/stripping CEs evaluated by Li||Cu coin cells at 0.5 mA cm^{-2} and 1 mA h cm^{-2}. Inset is the enlarged figure of CEs. **b**, Cycling stability demonstrated by Li plating/stripping in Li||Li symmetric cells at 0.5 mA cm^{-2} and 1.5 mA h cm^{-2}. **c**–**f**, SEM images illustrating the cross-section views (**c** and **e**) and the surface morphology (**d** and **f**) of the LMA collected from Li||NMC811 cells with the investigated electrolytes after 100 cycles at 0.5 C. **g**,**h**, SEI information obtained by the quantified atomic ratios of different elements by XPS conducted on the LMA after 100 cycles in 1 M $LiPF_6$/EC-EMC + 2% VC (**g**) and 1 m LiFSI/DMTMSA (**h**) electrolytes. Scale bars, 100 μm (**c**), 5 μm (**d** and **f**) and 10 μm (**e**).

from an initial thickness of 60 μm to ~250 μm (Fig. 6c). By contrast, the thickness increase was an order of magnitude less, and the less-compact layer was only ~26 μm thick (Fig. 6e), after cycling in our electrolyte. The Li particles remain larger, uniform and compact (Fig. 6f), while whisker-like Li deposits with high porosity can be observed in the case of the reference electrolyte (Fig. 6d).

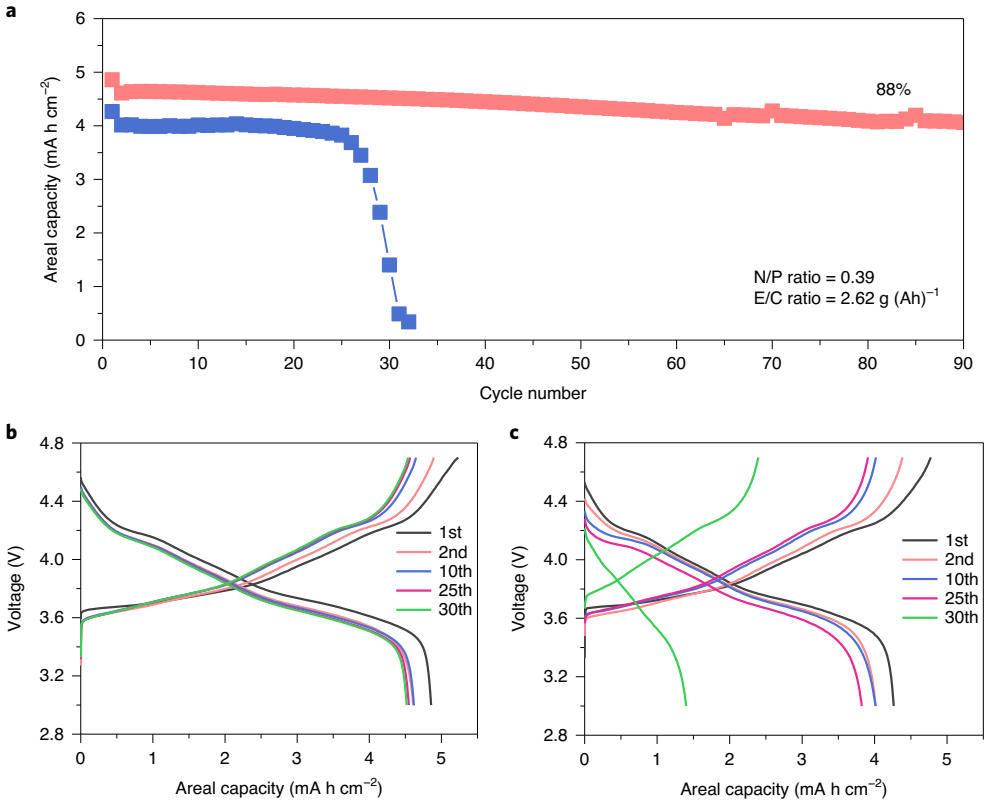

Fig. 7 | Electrochemical performance of Li || NMC811 cells under practical conditions. a–c, Cycling performance (**a**) and corresponding voltage profiles of the coin cells with high-loading NMC811 cathodes (>4 mA h cm^{-2}) at 4.7 V cut-off voltage using 1 m LiFSI/DMTMSA (**b**) and 1 M $LiPF_6$/EC-EMC + 2% VC (**c**) electrolytes. The discharging/charging rates were 0.1 C/0.1 C for the first cycle and 0.5 C/0.15 C afterwards. For 1 m LiFSI/DMTMSA electrolyte, the N/P and E/C ratios were ~0.39 and ~2.62 (g (Ah)$^{-1}$). For 1 M $LiPF_6$/EC-EMC + 2% VC electrolyte, the N/P ratio was ~2.8 (60 μm Li foil was used) and the E/C ratio was ~ 5 g (Ah)$^{-1}$.

Moreover, different SEI compositions formed in the different electrolytes were also identified by XPS on the cycled LMA (Fig. 6g,h). It is apparent that the SEI derived from the sulfonamide-based electrolyte was mainly composed of inorganic components including LiF and lower-valence sulfur (S^-/S^{2-}) species, which are preferable SEI components[12], while that derived from the carbonate reference electrolyte was abundant with organic components (Supplementary Fig. 18). Compared to the C–C and C–O/C=O groups in carbonates, the sulfonamide group (CF_3SO_2N–) facilitates the donation of F and S to the highly reductive Li to form more favourable SEIs.

Full-cell performance under practical conditions

To maximize the full-cell E_g for LMBs, high-loading cathode, lean electrolyte and a low amount of LMA should be used simultaneously[3], which is a great challenge. When using the reference electrolyte, 4.7 V LMBs with a high-loading NMC811 cathode (~4.25 mA h cm^{-2}), thin Li foil (60 μm; N/P ratio ~2.82) and limited electrolyte (E/C ratio ~5 g (Ah)$^{-1}$) can survive only 25 cycles (Fig. 7a), where uncontrolled side reactions rapidly deplete the Li and/or electrolyte and cause catastrophic capacity decay (Fig. 7c). Remarkably, even under much harsher conditions (cathode loading of ~4.86 mA h cm^{-2}, N/P ratio of ~0.39, E/C ratio of ~2.62 g (Ah)$^{-1}$), our 1 m LiFSI/DMTMSA electrolyte enables 4.7 V LMBs with greatly improved cycling stability, achieving 88% capacity retention after 90 cycles at a 0.5 C/0.15 C discharge/charge rate (Fig. 7a,b and Supplementary Fig. 19).

Higher-rate cycling data are available in Supplementary Fig. 20, where ~0.3 C charging offers good cycling performance with a cathode loading of ~3.5 mA h cm^{-2}, N/P ratio of ~1, E/C ratio of ~3.0 g (Ah)$^{-1}$ and ~0.5 C charging. To validate the achievable energy density, single-layer pouch cells were assembled and tested with different electrolytes with a cathode loading of ~18.4 mg cm^{-2}, E/C ratio of ~2.3 g (Ah)$^{-1}$ and N/P ratio of ~2.9 between 3.0 V and 4.7 V (Supplementary Fig. 21). The pouch cell with our electrolyte can stably deliver a specific energy of 353 W h kg^{-1} (Supplementary Table 4), while the one with the reference electrolyte rapidly degrades within 20 cycles. Adapting the parameters of demonstrated multilayer pouch cells[3], we estimate a cell-level specific energy of 417 W h kg^{-1} (Supplementary Table 5), which is encouraging for future development and large-scale production, and which reduces the cost (the present material costs are listed in Supplementary Table 6) of our sulfonamide electrolyte for practical high-voltage Li || NMC811 batteries.

Discussion

In the above, we presented the greatly improved electrochemical performance offered by our 1 m LiFSI in DMTMSA electrolyte and proved that it successfully modified cathode–electrolyte and anode–electrolyte interactions with suppressed side reactions. These findings lead to the interesting question of what the electrolyte does at the atomic level. On the anode side, weakly solvating electrolyte has been proposed[31,49] to weaken Li^+–solvent interactions while promoting Li^+–anion interactions. This creates more anion-derived SEIs, which are believed to benefit graphite[49] and LMA[31]. Our solvent DMTMSA has a weak solvation ability for salts[34] because of its low polarity[33], which together with the benefits of LiFSI makes

our 1 m LiFSI/DMTMSA electrolyte highly compatible with LMA. Meanwhile, our electrolyte has lower solubility of salts in general (compared to a carbonate electrolyte with higher polarity), including $Ni(TFSI)_2$, $Co(TFSI)_2$ and $Mn(TFSI)_2$, which have a TFSI group that is similar to that of the DMTMSA solvent (Supplementary Fig. 22). Such lowered solubilities are also expected for $Ni^{2+}/Co^{2+}/Mn^{2+}$ salts with other anion groups.

This lowered solubility could also explain the suppressed Al corrosion in the present study, because if the side reaction products between Al and LiFSI cannot be dissolved and diffuse away, they can become supersaturated and form an all-covering passivation layer (for example, the AlO_xF_y-like surface layer detected by XPS in Supplementary Fig. 8). And we note two additional advantages for our electrolyte compared to the carbonate ones. On one hand, EC is easy to dehydrogenate on highly delithiated NMC surfaces to form protic species, which could further react with $LiPF_6$ to generate corrosive HF[50]. By contrast, DMTMSA can avoid this issue due to its aprotic nature and good oxidation stability. On the other hand, LiFSI is more resistant to hydrolysis than $LiPF_6$ is (Supplementary Fig. 1d). All these effects should contribute to suppressed side reactions and better passivation.

Moreover, considering the SCC mechanism, the chemical corrosion attack is intensified by slippage and residual stress at grain boundaries, especially at the intergranular crack tip (Fig. 5a). It would in turn trigger faster crack propagation and catastrophic failure. However, such an issue can be largely relieved in our electrolyte, because it is less reactive (good oxidation stability) and corrosive (less HF), and the supersaturated side reaction products could not diffuse away in the nano-channel near the crack tip (Fig. 5a). It would modify the thermodynamics and kinetics of the cathode–electrolyte side reactions in a highly non-linear fashion, thus protecting the NMC811 secondary-particle architecture from intergranular SCC, driven by the cyclic grain-level anisotropic strains from lithiation/delithiation even at an extreme voltage of 4.7 V (0.94 Li removal per $LiTMO_2$).

Conclusions

To conclude, we demonstrated a sulfonamide-based electrolyte (1 m LiFSI in DMTMSA) for LMBs paired with ultra-high-voltage NMC811 cathodes that displays superior cycling stability under harsh conditions. On the cathode side, our electrolyte can successfully enable the stable cycling of 4.7 V NMC811, delivering a specific capacity of >230 mA h g^{-1} and an average CE of >99.65% over 100 cycles. Our electrolyte effectively stabilizes the NMC811 cathode surface, thus suppressing the rates of side reactions, gas evolution and TM dissolution. Detailed surface characterizations also suggest the formation of more LiF-like inorganic components inside the CEIs derived from our electrolyte compared to a commercial carbonate reference electrolyte. Moreover, the delayed intergranular SCC of NMC811 preserves electronic contacts between primary particles and prevents the need for more liquid electrolyte for wetting mode-I crack-generated fresh surfaces. On the LMA side, our electrolyte shows excellent compatibility with a desirable deposition morphology and minimized Li metal pulverization. Benefiting both electrodes of the full cell, the 1 m LiFSI/DMTMSA electrolyte enabled good cycling stability of ultra-high-voltage LMBs under industrially practical, harsh conditions. The findings of this study highlight the pivotal role of electrode–electrolyte interactions and recapitulate the tried-and-true 'electrolyte' approach for the future development of high-energy-density LMBs.

Methods

Materials. NMC811 cathodes were provided by Argonne National Laboratory with an areal loading of active materials of ~7.5 mg cm^{-2}. NMC811 powder (with LiB_xO_y coating; Supplementary Fig. 23), conductive carbon (Super C65) and 60-μm-thick Li on Cu foil were purchased from Targray, MTI and China Energy Lithium, respectively. Commercial electrolytes—1 M $LiPF_6$ in 3:7 (by weight) EC/EMC + 2 wt% VC and 1 M $LiPF_6$ in 3:7 (by weight) EC/EMC—were purchased from Soulbrain and BASF, respectively. LiFSI salt was supplied by KISCO. $Ni(TFSI)_2$, $Co(TFSI)_2$ and $Mn(TFSI)_2$ were purchased from Sigma Aldrich. DMTMSA was synthesized following our previously reported procedure[34]. Possible residual water was removed from the salt and as-received solvent by heat treatment under vacuum and molecular sieves before use, respectively. Molality (m, moles of salt in kilograms of solvent (mol kg^{-1})) and molarity (M, moles of salt in litres of solution (mol l^{-1})) are used to denote the salt concentration in electrolytes. No other ingredient was employed in our sulfonamide-based electrolyte as additive.

Characterizations. Cycled Li and NMC811 electrodes were obtained by disassembling CR2032 coin cells in the glove box with O_2 and H_2O level <1 ppm, and then washing them with pure dimethyl ether (DME) and dimethyl carbonate (DMC), respectively. The morphology and microstructure were obtained from high-resolution SEM (Zeiss Merlin) and TEM (JOEL 2010F). Thin-section TEM specimens were fabricated directly from the cycled NMC811 electrode by a standard lift-out procedure[43] by focused ion beam (NVision 40 CrossBeam, ZEISS). The surface chemistry of cycled electrodes was analysed by XPS (Physical Electronics Versaprobe II) and TOF-SIMS (ION-TOF). Ex situ three-dimensional tomography and transmission X-ray microscopy XANES on the cycled NMC811 electrodes sealed in Kapton film were conducted on FXI beamline at National Synchrotron Light Source II of Brookhaven National Laboratory. The bulk XANES of these samples were measured in transmission mode using 20-BM-B beamline of Advanced Photon Source at Argonne National Laboratory. Whiteline peak position tracking method[51] (Supplementary Note) was used in transmission X-ray microscopy XANES data analysis where the whiteline peak positions represent the Ni oxidation states.

In situ DEMS was used for detecting the gas evolution during cell charging at 0.03 C using different electrolytes. Details on the instrument set-up can be found elsewhere[52]. For the TM dissolution measurement, coin cells with NMC811 as the cathode and Li metal foil as the anode in different electrolytes were first assembled. Then following an established method[18], ICP-MS (Agilent 7900) was used to determine the metal concentration. Cross-sections of cycled cathodes were cut by an ion-milling machine (IM-40000, Hitachi) and inspected by SEM. The solubility of $Ni(TFSI)_2$, $Co(TFSI)_2$ and $Mn(TFSI)_2$ in both electrolytes was measured in grams per 100 g. The purity of DMTMSA was analysed with ^1H and ^{19}F NMR. A 3,000 ppm water was added into the 1 M $LiPF_6$/EC-EMC + 2 wt% VC and 1 m LiFSI/DMTMSA electrolytes and aged for several days. The water contents in the electrolyte before and after ageing were measured by Karl Fisher titration (Metler-Toledo). The viscosity was measured using a SVM3001 viscometer (Anton Paar).

A conductivity cell with two platinum-black electrodes was used to measure the Li ion conductivity. Standard solution (0.01 M KCl aqueous solution, 1.41 mS cm^{-1}) was used to calibrate the cell constant. The conductivity cell was immersed into electrolyte and the Li ion conductivity was measured by the impedance method with a frequency ranging from 10^6 to 10^1 Hz (Gamry Reference 600+). The transference number of Li^+ (t_+) was evaluated by the method proposed by Bruce and Vincent[53]. For evaluating the wettability of different electrolytes, the electrolyte was first dropped onto Celgard 2325 separator and then the contact angle was measured by a contact angle meter (SL200B, KINO Scientific Instrument).

Electrochemical measurements. CR2032 coin cells were prepared using NMC811 as the cathode, Celgard 2325 (polypropylene–polyethylene–polypropylene) as the separator and a Li metal anode in the glove box. For cathodes with high areal loading, NMC811, Super C65 and polyvinylidene fluoride binder in a weight ratio of 94:3:3 were first mixed with *N*-methyl-2-pyrrolidone to form a uniform slurry, which was coated onto Al foil using a doctor blade. The thickness was ~96 μm for the high-loading NMC811 cathode and ~52 μm for the low-loading NMC811 cathode, both including 15-μm-thick Al foil. The porosity was ~33% for the high-loading NMC811 cathode and ~36% for the low-loading NMC811 cathode. Then the coated electrodes were dried at 120 °C overnight. Finally, the electrodes were rolled and punched.

Li metal foils with 350 μm and 60 μm (on Cu) were used. The Li anode paired with high-loading NMC811 cathodes in the coin cell was fabricated by electrochemical deposition on Cu foil without pretreatment. Electrolyte amounts in coin cells were carefully controlled by pipette. Landt CT 2001A and BTS9000 Neware cyclers were used to perform galvanostatic cycling at different C rates (1 C is 200 mA g^{-1}). The galvanostatic intermittent titration technique was performed on cycled coin cells within a voltage range of ~3.0–4.7 V with current pulse intervals at ~0.5 C for 8 minutes, followed by 60-minute rests. The electrochemical floating test was performed in coin cells with NMC811 and Li metal as cathode and anode, respectively, in different electrolytes. The cells were first charged to 4.7 V at 0.1 C and then maintained for 20 h with the current monitored by the Neware cycler.

The cathodes for SEM observation after the floating test were collected by dissembling the cells and then washing with DMC three times. The electrochemical stability of electrolytes was evaluated by a linear sweep voltammetry method at a scan rate of 10 mV s^{-1} using a Li || Al configuration. The stability of the Al current collector in different electrolytes at high voltages was

measured by a Li || Al configuration while holding the potential at 4.7 V for 10 h. Then the Al foils were collected and characterized by SEM and XPS. Single-layer pouch cell was assembled by hand-stacking the NMC811 cathode, Li foil (on Cu current collector) and separator, followed by electrolyte injecting and vacuum sealing. The gravimetric energy density of the jellyroll pouch cell was calculated based on the mass of cathode, anode, separator and electrolyte.

Data availability

The datasets analysed and generated during the current study are included in the paper and its Supplementary Information.

Received: 7 May 2020; Accepted: 9 February 2021;
Published online: 25 March 2021

References

1. Li, W., Erickson, E. M. & Manthiram, A. High-nickel layered oxide cathodes for lithium-based automotive batteries. *Nat. Energy* **5**, 26–34 (2020).
2. Xue, W. et al. Intercalation-conversion hybrid cathodes enabling Li–S full-cell architectures with jointly superior gravimetric and volumetric energy densities. *Nat. Energy* **4**, 374–382 (2019).
3. Liu, J. et al. Pathways for practical high-energy long-cycling lithium metal batteries. *Nat. Energy* **4**, 180–186 (2019).
4. Xue, W. et al. Gravimetric and volumetric energy densities of lithium-sulfur batteries. *Curr. Opin. Electrochem.* **6**, 92–99 (2017).
5. Manthiram, A., Song, B. & Li, W. A perspective on nickel-rich layered oxide cathodes for lithium-ion batteries. *Energy Storage Mater.* **6**, 125–139 (2017).
6. Noh, H.-J., Youn, S., Yoon, C. S. & Sun, Y.-K. Comparison of the structural and electrochemical properties of layered $Li[Ni_xCo_yMn_z]O_2$ (x=1/3, 0.5, 0.6, 0.7, 0.8 and 0.85) cathode material for lithium-ion batteries. *J. Power Sources* **233**, 121–130 (2013).
7. Ren, X. et al. Enabling high-voltage lithium-metal batteries under practical conditions. *Joule* **3**, 1662–1676 (2019).
8. Niu, C. et al. Self-smoothing anode for achieving high-energy lithium metal batteries under realistic conditions. *Nat. Nanotechnol.* **14**, 594–601 (2019).
9. Li, W., Song, B. & Manthiram, A. High-voltage positive electrode materials for lithium-ion batteries. *Chem. Soc. Rev.* **46**, 3006–3059 (2017).
10. Ahmed, S. et al. Cost of automotive lithium-ion batteries operating at high upper cutoff voltages. *J. Power Sources* **403**, 56–65 (2018).
11. Jung, R., Metzger, M., Maglia, F., Stinner, C. & Gasteiger, H. A. Chemical versus electrochemical electrolyte oxidation on NMC111, NMC622, NMC811, LNMO, and conductive carbon. *J. Phys. Chem. Lett.* **8**, 4820–4825 (2017).
12. Xue, W. et al. FSI-inspired solvent and 'full fluorosulfonyl' electrolyte for 4 V class lithium-metal batteries. *Energy Environ. Sci.* **13**, 212–220 (2020).
13. Suo, L. et al. Fluorine-donating electrolytes enable highly reversible 5-V-class Li metal batteries. *Proc. Natl Acad. Sci. USA* **115**, 1156–1161 (2018).
14. Ma, L., Nie, M., Xia, J. & Dahn, J. R. A systematic study on the reactivity of different grades of charged $Li[Ni_xMn_yCo_z]O_2$ with electrolyte at elevated temperatures using accelerating rate calorimetry. *J. Power Sources* **327**, 145–150 (2016).
15. Jung, R., Metzger, M., Maglia, F., Stinner, C. & Gasteiger, H. A. Oxygen release and its effect on the cycling stability of $LiNi_xMn_yCo_zO_2$(NMC) cathode materials for Li-ion batteries. *J. Electrochem. Soc.* **164**, A1361–A1377 (2017).
16. Laszczynski, N., Solchenbach, S., Gasteiger, H. A. & Lucht, B. L. Understanding electrolyte decomposition of graphite/NCM811 cells at elevated operating voltage. *J. Electrochem. Soc.* **166**, A1853–A1859 (2019).
17. Ryu, H.-H., Park, K.-J., Yoon, C. S. & Sun, Y.-K. Capacity fading of Ni-rich $Li[Ni_xCo_yMn_{1-x-y}]O_2$ ($0.6 \le x \le 0.95$) cathodes for high-energy-density lithium-ion batteries: bulk or surface degradation? *Chem. Mater.* **30**, 1155–1163 (2018).
18. Xu, G.-L. et al. Building ultraconformal protective layers on both secondary and primary particles of layered lithium transition metal oxide cathodes. *Nat. Energy* **4**, 484–494 (2019).
19. Li, W., Kim, U. H., Dolocan, A., Sun, Y. K. & Manthiram, A. Formation and inhibition of metallic lithium microstructures in lithium batteries driven by chemical crossover. *ACS Nano* **11**, 5853–5863 (2017).
20. Xue, W. et al. Manipulating sulfur mobility enables advanced Li-S batteries. *Matter* **1**, 1047–1060 (2019).
21. Xue, W. et al. Double-oxide sulfur host for advanced lithium-sulfur batteries. *Nano Energy* **38**, 12–18 (2017).
22. Li, S. et al. Developing high-performance lithium metal anode in liquid electrolytes: challenges and progress. *Adv. Mater.* **30**, 1706375 (2018).
23. Kushima, A. et al. Liquid cell transmission electron microscopy observation of lithium metal growth and dissolution: root growth, dead lithium and lithium flotsams. *Nano Energy* **32**, 271–279 (2017).
24. Xu, H. et al. Surpassing lithium metal rechargeable batteries with self-supporting Li–Sn–Sb foil anode. *Nano Energy* **74**, 104815 (2020).
25. Tatara, R. et al. Enhanced cycling performance of Ni-rich positive electrodes (NMC) in Li-ion batteries by reducing electrolyte free-solvent activity. *ACS Appl. Mater. Interfaces* **11**, 34973–34988 (2019).
26. Fan, X. et al. Highly fluorinated interphases enable high-voltage Li-metal batteries. *Chem* **4**, 174–185 (2018).
27. Chen, S. et al. High-voltage lithium-metal batteries enabled by localized high-concentration electrolytes. *Adv. Mater.* **30**, 1706102 (2018).
28. Fan, X. et al. All-temperature batteries enabled by fluorinated electrolytes with non-polar solvents. *Nat. Energy* **4**, 882–890 (2019).
29. Fan, X. et al. Non-flammable electrolyte enables Li-metal batteries with aggressive cathode chemistries. *Nat. Nanotechnol.* **13**, 715–722 (2018).
30. Cao, X. et al. Monolithic solid–electrolyte interphases formed in fluorinated orthoformate-based electrolytes minimize Li depletion and pulverization. *Nat. Energy* **4**, 796–805 (2019).
31. Yu, Z. et al. Molecular design for electrolyte solvents enabling energy-dense and long-cycling lithium metal batteries. *Nat. Energy* **5**, 526–533 (2020).
32. Zheng, Q. et al. A cyclic phosphate-based battery electrolyte for high voltage and safe operation. *Nat. Energy* **5**, 291–298 (2020).
33. Shyamsunder, A. et al. Inhibiting polysulfide shuttle in lithium–sulfur batteries through low-ion-pairing salts and a triflamide solvent. *Angew. Chem. Int. Ed.* **56**, 6192–6197 (2017).
34. Feng, S. et al. Molecular design of stable sulfamide- and sulfonamide-based electrolytes for aprotic Li-O_2 batteries. *Chem* **5**, 2630–2641 (2019).
35. Kim, U. H. et al. Microstructure-controlled Ni-rich cathode material by microscale compositional partition for next-generation electric vehicles. *Adv. Energy Mater.* **9**, 1803902 (2019).
36. Park, G.-T., Ryu, H.-H., Park, N.-Y., Yoon, C. S. & Sun, Y.-K. Tungsten doping for stabilization of $Li[Ni_{0.90}Co_{0.05}Mn_{0.05}]O_2$ cathode for Li-ion battery at high voltage. *J. Power Sources* **442**, 227242 (2019).
37. Eftekhari, A. Energy efficiency: a critically important but neglected factor in battery research. *Sustain. Energy Fuels* **1**, 2053–2060 (2017).
38. Pritzl, D., Solchenbach, S., Wetjen, M. & Gasteiger, H. A. Analysis of vinylene carbonate (VC) as additive in graphite/$LiNi_{0.5}Mn_{1.5}O_4$ cells. *J. Electrochem. Soc.* **164**, A2625–A2635 (2017).
39. Ma, T. et al. Revisiting the corrosion of the aluminum current collector in lithium-ion batteries. *J. Phys. Chem. Lett.* **8**, 1072–1077 (2017).
40. Sun, H.-H. & Manthiram, A. Impact of microcrack generation and surface degradation on a nickel-rich layered $Li[Ni_{0.9}Co_{0.05}Mn_{0.05}]O_2$ cathode for lithium-ion batteries. *Chem. Mater.* **29**, 8486–8493 (2017).
41. Liu, H. et al. Intergranular cracking as a major cause of long-term capacity fading of layered cathodes. *Nano Lett.* **17**, 3452–3457 (2017).
42. Li, W., Dolocan, A., Li, J., Xie, Q. & Manthiram, A. Ethylene carbonate-free electrolytes for high-nickel layered oxide cathodes in lithium-ion batteries. *Adv. Energy Mater.* **9**, 1901152 (2019).
43. Yan, P. et al. Tailoring grain boundary structures and chemistry of Ni-rich layered cathodes for enhanced cycle stability of lithium-ion batteries. *Nat. Energy* **3**, 600–605 (2018).
44. Kim, J. et al. Controllable solid electrolyte interphase in nickel-rich cathodes by an electrochemical rearrangement for stable lithium-ion batteries. *Adv. Mater.* **30**, 1704309 (2018).
45. Cha, H. et al. Boosting reaction homogeneity in high-energy lithium-ion battery cathode materials. *Adv. Mater.* **32**, 2003040 (2020).
46. Zhang, F. et al. Surface regulation enables high stability of single-crystal lithium-ion cathodes at high voltage. *Nat. Commun.* **11**, 3050 (2020).
47. Friedrich, F. et al. Capacity fading mechanisms of NCM-811 cathodes in lithium-ion batteries studied by X-ray diffraction and other diagnostics. *J. Electrochem. Soc.* **166**, A3760–A3774 (2019).
48. Xu, R., Sun, H., de Vasconcelos, L. S. & Zhao, K. Mechanical and structural degradation of $LiNi_xMn_yCo_zO_2$ cathode in Li-ion batteries: an experimental study. *J. Electrochem. Soc.* **164**, A3333–A3341 (2017).
49. Yao, Y.-X. et al. Regulating interfacial chemistry in lithium-ion batteries by a weakly-solvating electrolyte. *Angew. Chem. Int. Ed.* **60**, 4090–4097 (2020).
50. Yu, Y. et al. Coupled $LiPF_6$ decomposition and carbonate dehydrogenation enhanced by highly covalent metal oxides in high-energy Li-ion batteries. *J. Phys. Chem. C* **122**, 27368–27382 (2018).
51. Wolf, M., May, B. M. & Cabana, J. Visualization of electrochemical reactions in battery materials with X-ray microscopy and mapping. *Chem. Mater.* **29**, 3347–3362 (2017).
52. Yu, Y. et al. Revealing electronic signatures of lattice oxygen redox in lithium ruthenates and implications for high-energy Li-ion battery material designs. *Chem. Mater.* **31**, 7864–7876 (2019).
53. Evans, J., Vincent, C. A. & Bruce, P. G. Electrochemical measurement of transference numbers in polymer electrolytes. *Polymer* **28**, 2324–2328 (1987).

Acknowledgements

We acknowledge support by the Department of Energy, Basic Energy Sciences, under award number DE-SC0002633 (Chemomechanics of Far-From-Equilibrium Interfaces). We acknowledge the cathodes provided by the US Department of Energy CAMP Facility, Argonne National Laboratory, and the LiFSI salt by KISCO. This work made use of

the Material Research Science and Engineering Center Shared Experimental Facilities supported by the National Science Foundation under award number DMR-1419807. Z.S. acknowledges the research grant at the Department of Materials Science and Engineering at the Massachusetts Institute of Technology. This work used resources of the beamline FXI/18ID of the National Synchrotron Light Source II, a US Department of Energy Office of Science User Facility operated for the Department of Energy Office of Science by Brookhaven National Laboratory under contract no. DE-SC0012704. This work used resources of the Advanced Photon Source, an Office of Science User Facility operated for the US Department of Energy Office of Science by Argonne National Laboratory, and was supported by the US Department of Energy under contract no. DE-AC02-06CH11357 and the Canadian Light Source and its funding partners. J. Lopez acknowledges support by an appointment to the Intelligence Community Postdoctoral Research Fellowship Program at the Massachusetts Institute of Technology, administered by Oak Ridge Institute for Science and Education through an interagency agreement between the US Department of Energy and the Office of the Director of National Intelligence. We also thank C. Mao at Zhu Hai Smooth Way Company for valuable suggestions and G. Leverick from Y. Shao-Horn's group at the Massachusetts Institute of Technology for the support in measuring the water content by Karl Fisher titration.

Author contributions

W.X., Y.D., J.A.J., Y.S.-H. and J. Li conceived the concept and the project. M.H., W.Z. and S.L. synthesized the solvent. W.X. designed the electrolyte and conducted electrochemical measurements. Y.L. conducted TOF-SIMS measurements and analysed the results. Y.G.Z. conducted in situ DEMS measurements. R.G. conducted focused ion beam and TEM analysis. W.X., X.X., D.Y., Z.S., C-J.S., I.H. and W.-K.L. conducted in situ synchrotron-based FXI measurements and analysed the results. P.L. conducted ICP-MS measurements. W.X., G.X., J. Lopez, W.F. and R.X. conducted other characterizations. W.X., Y.D., Y.Y., Y.S.-H, J.A.J. and J. Li wrote and revised the manuscript. All authors discussed the results and reviewed the manuscript.

Competing interests

The authors declare no competing interests.

Additional information

Supplementary information The online version contains supplementary material available at https://doi.org/10.1038/s41560-021-00792-y.

Correspondence and requests for materials should be addressed to Y.D., Y.S.-H., J.A.J. or J.L.

Peer review information *Nature Energy* thanks Corsin Battaglia and the other, anonymous, reviewer(s) for their contribution to the peer review of this work.

Reprints and permissions information is available at www.nature.com/reprints.

Publisher's note Springer Nature remains neutral with regard to jurisdictional claims in published maps and institutional affiliations.

nature portfolio

https://doi.org/10.1038/s41560-021-00792-y

Supplementary information

Ultra-high-voltage Ni-rich layered cathodes in practical Li metal batteries enabled by a sulfonamide-based electrolyte

In the format provided by the authors and unedited

Ultra-high-voltage Ni-rich layered cathodes in practical lithium-metal batteries enabled by a sulfonamide-based electrolyte

Weijiang Xue[1], Mingjun Huang[2], Yutao Li[3], Yun Guang Zhu[4], Rui Gao[1], Xianghui Xiao[5], Wenxu Zhang[2], Sipei Li[4], Guiyin Xu[1], Yang Yu[6], Peng Li[1], Jeffrey Lopez[4], Daiwei Yu[7], Yanhao Dong[1,*], Weiwei Fan[1], Zhe Shi[6], Rui Xiong[1,8], Chengjun Sun[9], Inhui Hwang[9], Wah-Keat Lee[5], Yang Shao-Horn[4,6,10,*], Jeremiah A. Johnson[2,*], Ju Li[1,6,*]

[1] Department of Nuclear Science and Engineering, Massachusetts Institute of Technology, Cambridge, Massachusetts 02139, USA

[2] Department of Chemistry, Massachusetts Institute of Technology, Cambridge, Massachusetts 02139, USA

[3] Materials Science and Engineering Program and Texas Materials Institute, The University of Texas at Austin, Austin, TX 78712, USA

[4] Research Laboratory of Electronics, Massachusetts Institute of Technology, Cambridge, MA 02139, USA

[5] National Synchrotron Light Source II, Brookhaven National Laboratory, Upton, NY 11973

[6] Department of Materials Science and Engineering, Massachusetts Institute of Technology, Cambridge, Massachusetts 02139, USA

[7] Department of Electrical Engineering and Computer Science, Massachusetts Institute of Technology, Cambridge, Massachusetts 02139, USA

[8] National Engineering Laboratory for Electric Vehicles, School of Mechanical Engineering, Beijing Institute of Technology, Beijing 100081, China

[9] Advanced Photon Source, Argonne National Laboratory, Lemont, IL 60439

[10] Department of Mechanical Engineering, Massachusetts Institute of Technology, Cambridge, Massachusetts 02139, USA

*Corresponding authors. Email: dongyh@mit.edu (Y.D.), shaohorn@mit.edu (Y.S.H.), jaj2109@mit.edu (J.A.J.), liju@mit.edu (J. Li).

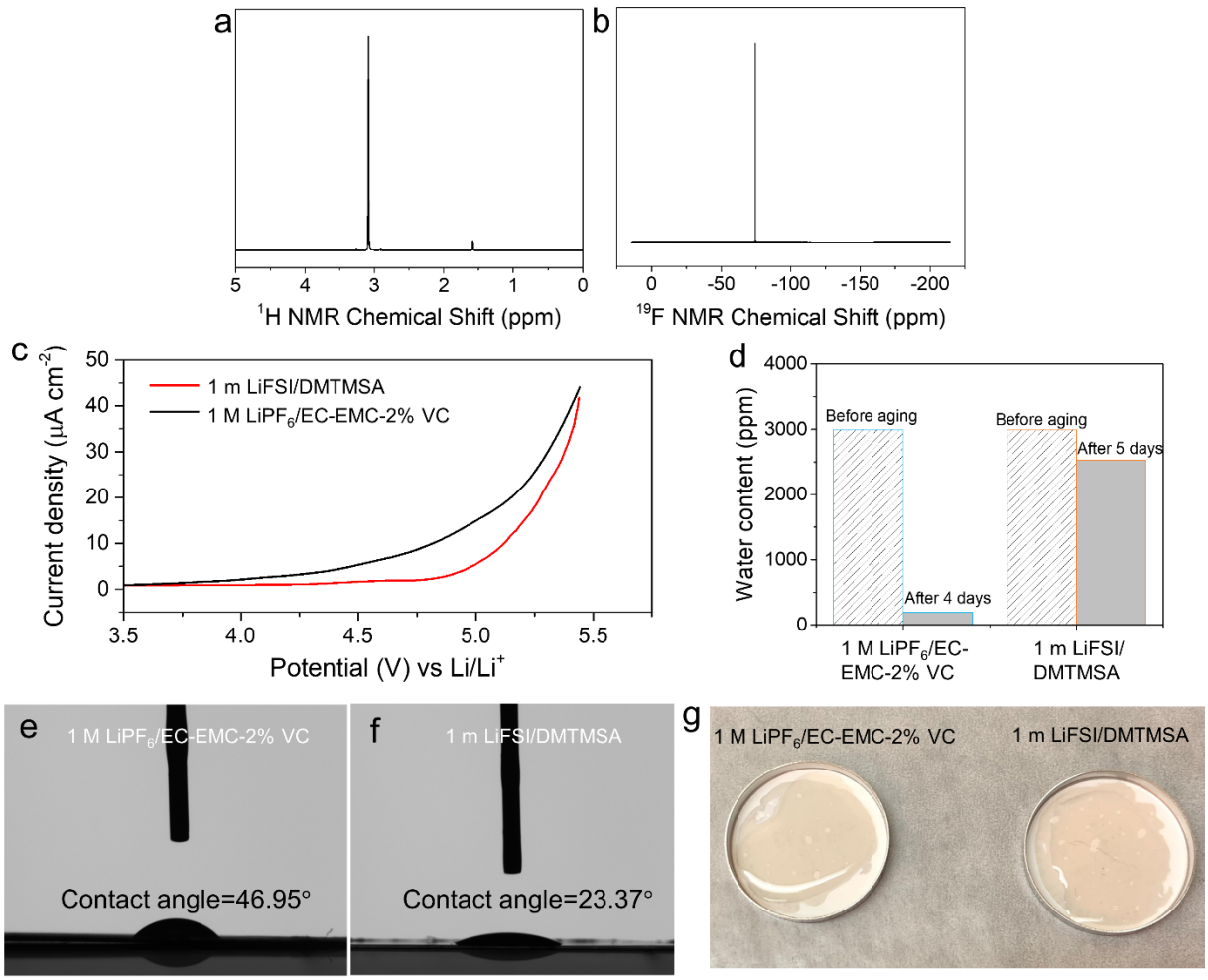

Supplementary Figure 1 Characterizations of the DMTMSA solvent, 1 m LiFSI/DMTMSA and 1 M $LiPF_6$/EC-EMC-2% VC electrolytes. ^{1}H NMR (a) and ^{19}F NMR (b) of the as-synthesized DMTMSA solvent. Electrochemical stability (c), water contents in different electrolytes with adding 3000 ppm water before and after aging (d), contact angles (e, f) and optical images of electrolytes dropped on the separators (g) of 1 M $LiPF_6$/EC-EMC-2% VC and 1 m LiFSI/DMTMSA electrolytes.

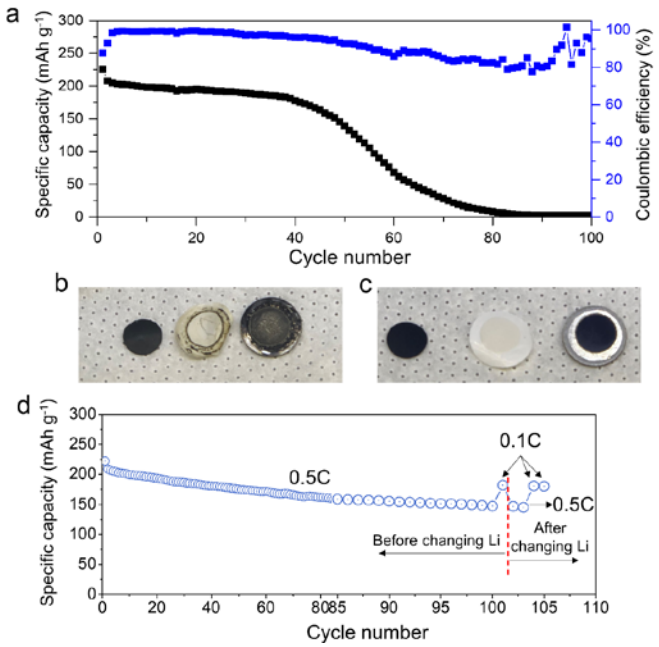

Supplementary Figure 2 Cycling performance of Li||NMC811 cells with the 1 M $LiPF_6$/EC-EMC+2% VC electrolyte with different Li anode excess and electrolyte amounts with 3.0 V~4.7 V at 0.5 C. (a) Thin Li foil (60 μm thick) and limited amount of electrolyte (20 μL) were used. Optical figures of the cathode, separator and Li metal disassembled from the cells with the 1 M $LiPF_6$/EC-EMC+2% VC (b, corresponding to a) and 1 m LiFSI/DMTMSA (c) electrolytes after 100 cycles at 0.5 C. (d) Superabundant Li (350 μm) and electrolyte (80 μL) were used. After 100 cycles, the cycled Li-metal anode was changed to investigate if the capacity decay was from the Li anode side.

Under the stringent condition, the cell with the reference carbonate electrolyte has very poor performance with a sudden capacity drop after ~40 cycles, due to electrolyte compatibility issue with the LMA (Supplementary Figure 2a, b, c). After 100^{th} cycle, a lower charging-discharging rate of 0.1 C was used to examine the recovered specific capacity. Then the cycled NMC811 cathode was used to assemble a new cell with a fresh Li foil and electrolyte to exclude the effect of the counter electrode and electrolyte on the cycling performance. The new cell was charged-discharged at 0.5 C for two cycles followed by additional two cycles at 0.1 C. The specific capacities at both rates were almost identical to the ones before changing the Li metal indicating that the cycling behavior is dominated by the cathode itself under superabundant Li metal and electrolyte. In other words, we confirm that the degradation mainly comes from the cathode itself. Therefore, the intrinsic cathode performance should be investigated with superabundant electrolyte and Li metal for the carbonate reference electrolyte.

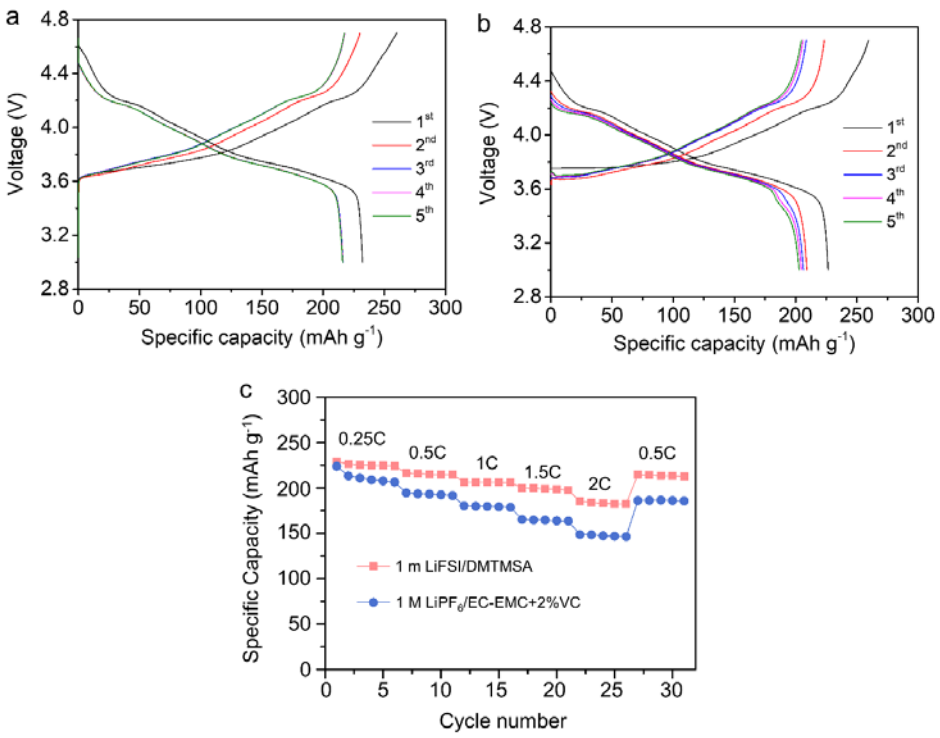

Supplementary Figure 3 Voltage profiles of the Li||NMC811 cells using 1 m LiFSI/DMTMSA (a) and 1 M $LiPF_6$/EC-EMC-2 %VC (b) electrolytes during 1^{st} ~ 5^{th} cycles. 0.1 C for the 1^{st} cycle and 0.5 C for the rest. (c) Rate performance of the cells using the investigated electrolytes (same charging and discharging rates were used).

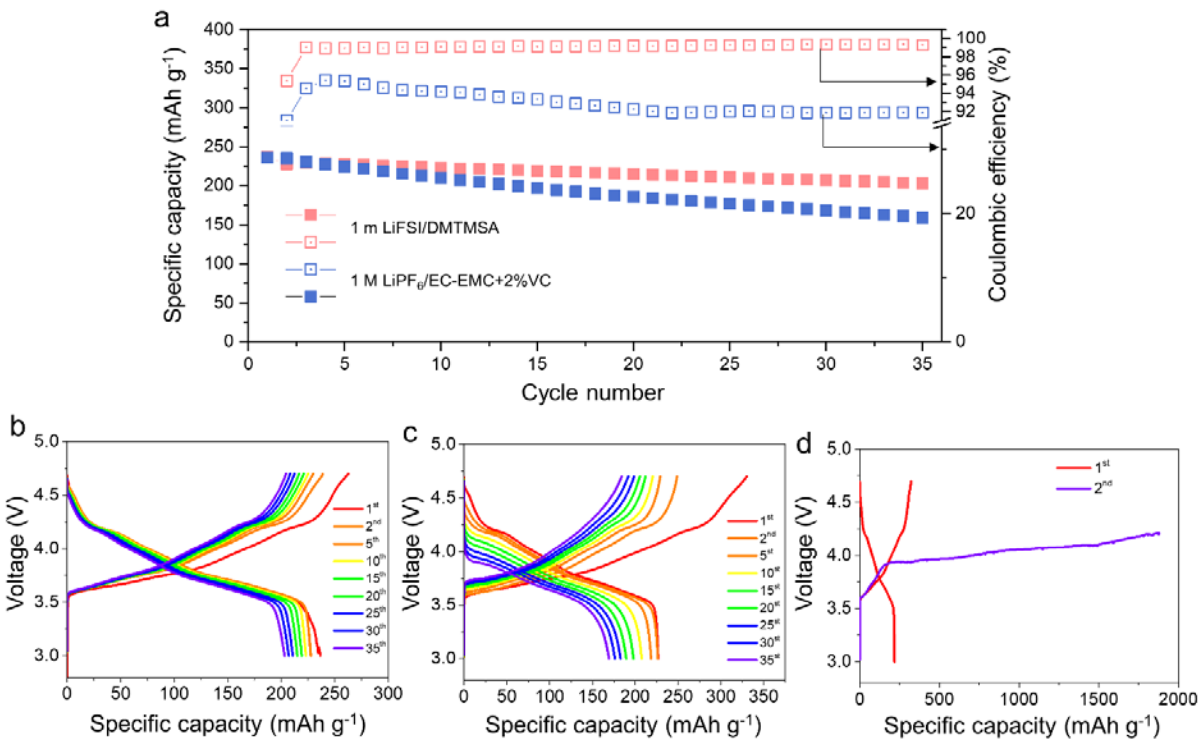

Supplementary Figure 4 High-temperature (55 ºC) cycling performance (a) and corresponding voltage profiles (b~d) of the Li||NMC811 cells using different electrolytes at 0.5 C. The cells were cycled between 3 V to 4.7 V. The electrolytes used in (b), (c) and (d) were 1 m LiFSI/DMTMSA, 1 M $LiPF_6$/EC-EMC and 1 M $LiPF_6$/EC-EMC+2% VC, respectively.

The cell using the 1 M $LiPF_6$/EC-EMC electrolyte (c) exhibited a poor cyclability and low CE of only ~92% while the one using 1 M $LiPF_6$/EC-EMC+2% VC could not be cycled due to continuous electrolyte decomposition of VC (d).

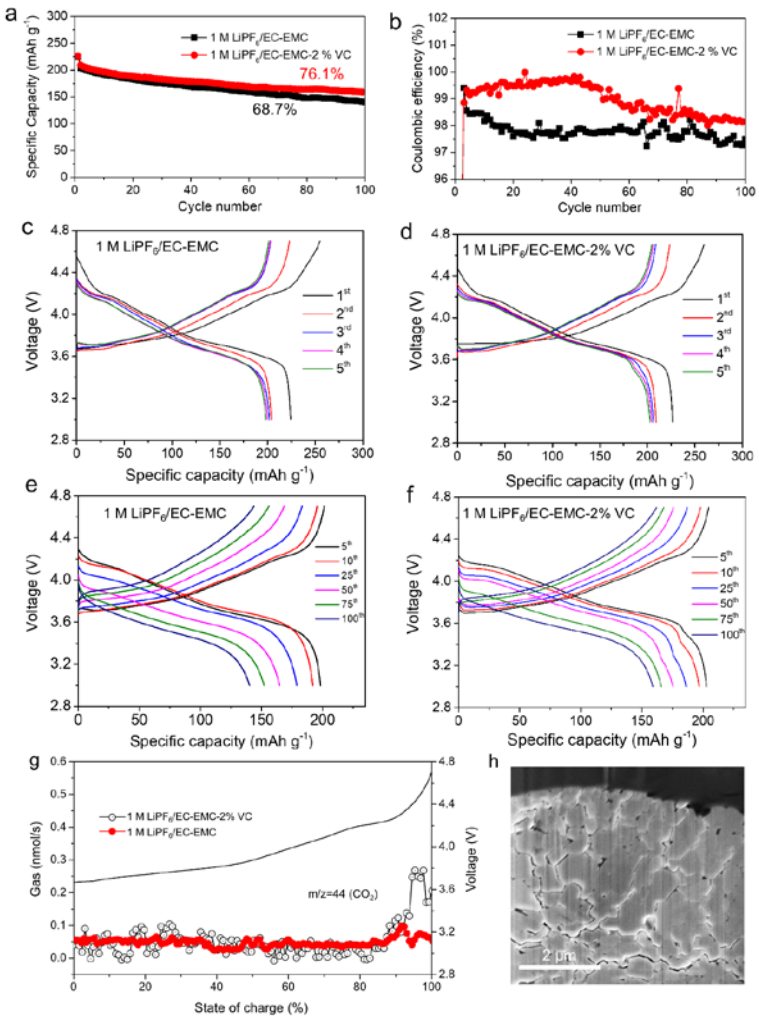

Supplementary Figure 5 Comparison between electrochemical performances with 1 M $LiPF_6$/EC-EMC+2% VC and 1 M $LiPF_6$/EC-EMC electrolytes. Cycling performances (a), Coulombic efficiencies (b) and corresponding voltage profiles for the first 5 (c, d) and following cycles (e, f). The cells were cycled between 3 V to 4.7 V. 350 µm Li foil and 80 µl electrolyte were used. Comparison between the CO_2 evolution during the 1st charge with electrolytes with/without VC (g). SEM images of the cross-section of the NMC811 cathode after 100 cycles in 1 M $LiPF_6$/EC-EMC electrolyte (h).

As shown in (a), the capacity retention of the cell with 1 M $LiPF_6$/EC-EMC electrolyte is 68.7%, worse than that with 1 M $LiPF_6$/EC-EMC+2% VC (76.1%) under the same testing conditions (a, b). The first-cycle CE of the cell using 1 M $LiPF_6$/EC-EMC+2% VC (87.2%, c) is lower than the one without VC (88.0%, d), probably due to some decomposition of VC during the first charge. However, the electrolyte with VC showed higher average CE (~99.5%) than the one without VC (~98%) for the first ~50 cycles (b), suggesting a positive role of the VC presence. We performed *in-situ* DEMS to monitor the CO_2 evolution

using 1 M $LiPF_6$/EC-EMC (3:7) electrolyte without VC and compared it to the electrolyte with VC. As shown in (g), although CO_2 evolution onsets at similar voltage in the two electrolytes, the one with VC has more CO_2 production above ~4.4 V vs. Li^+/Li. This can be attributed to the high-voltage decomposition of VC (*J. Electrochem. Soc.*, **164**, 2017, A2625-A2635). SEM images on FIB-sliced cross-section of the NMC811 cathode after 100 cycles in 1 M $LiPF_6$/EC-EMC electrolyte (h) also show severe cracking, similar to the one cycled in 1 M $LiPF_6$/EC-EMC+2% VC electrolyte. Therefore, the main observations in morphology and electrochemical performances with 1 M $LiPF_6$/EC-EMC electrolyte are similar as those with VC-contained electrolyte.

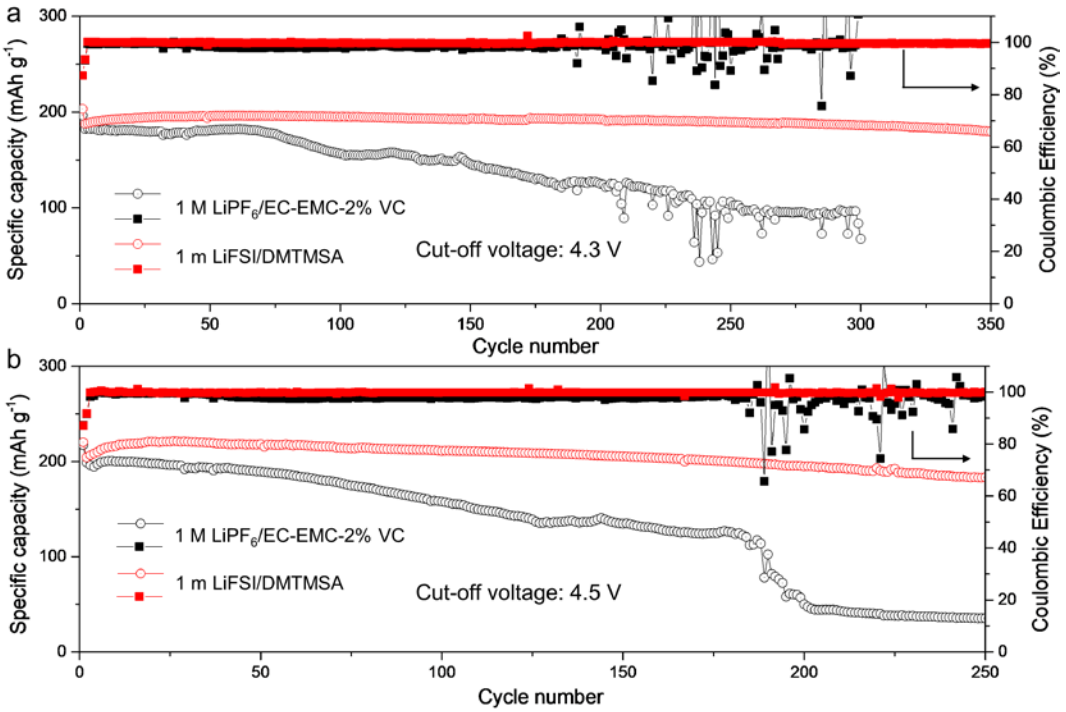

Supplementary Figure 6 Cycling performance of Li||NMC811 cells with cut-off voltages of 4.3 V (a) and 4.5 V (b) in 1 M $LiPF_6$/EC-EMC-2% VC and 1 m LiFSI/DMTMSA electrolytes. Rate: 0.1 C for the 1st cycle and 0.5 C for the rest cycles. For cells with 1 m LiFSI/DMTMSA electrolyte, "stringent conditions" (60 μm Li foil and 20 μL electrolyte) were used. For cells with 1 M $LiPF_6$/EC-EMC+2% VC electrolyte, "super-excessive conditions" (350 μm Li foil and 80 μL electrolyte) were used.

For the cell with 1 m LiFSI/DMTMSA electrolyte and 4.3 V cut-off voltage, the initial specific capacity was 203.3 mAh g^{-1} with a high average CE of 99.87% and capacity retention of 95.6% after 350 cycles. In contrast, the Li||NMC811 cell with 1 M $LiPF_6$/EC-EMC-2% VC electrolyte showed a much lower capacity retention of 37.1% after 300 cycles. When the cut-off voltage was elevated to 4.5 V, the capacity retention of the cell using 1 m LiFSI/DMTMSA electrolyte was as high as 89.3% after 250 cycles with a high initial specific capacity of 220.2 mAh g^{-1} and average CE of 99.87%. For the cell using the carbonate electrolyte, the capacity retention was only 63% after 170 cycles after which a sudden drop in capacity was observed.

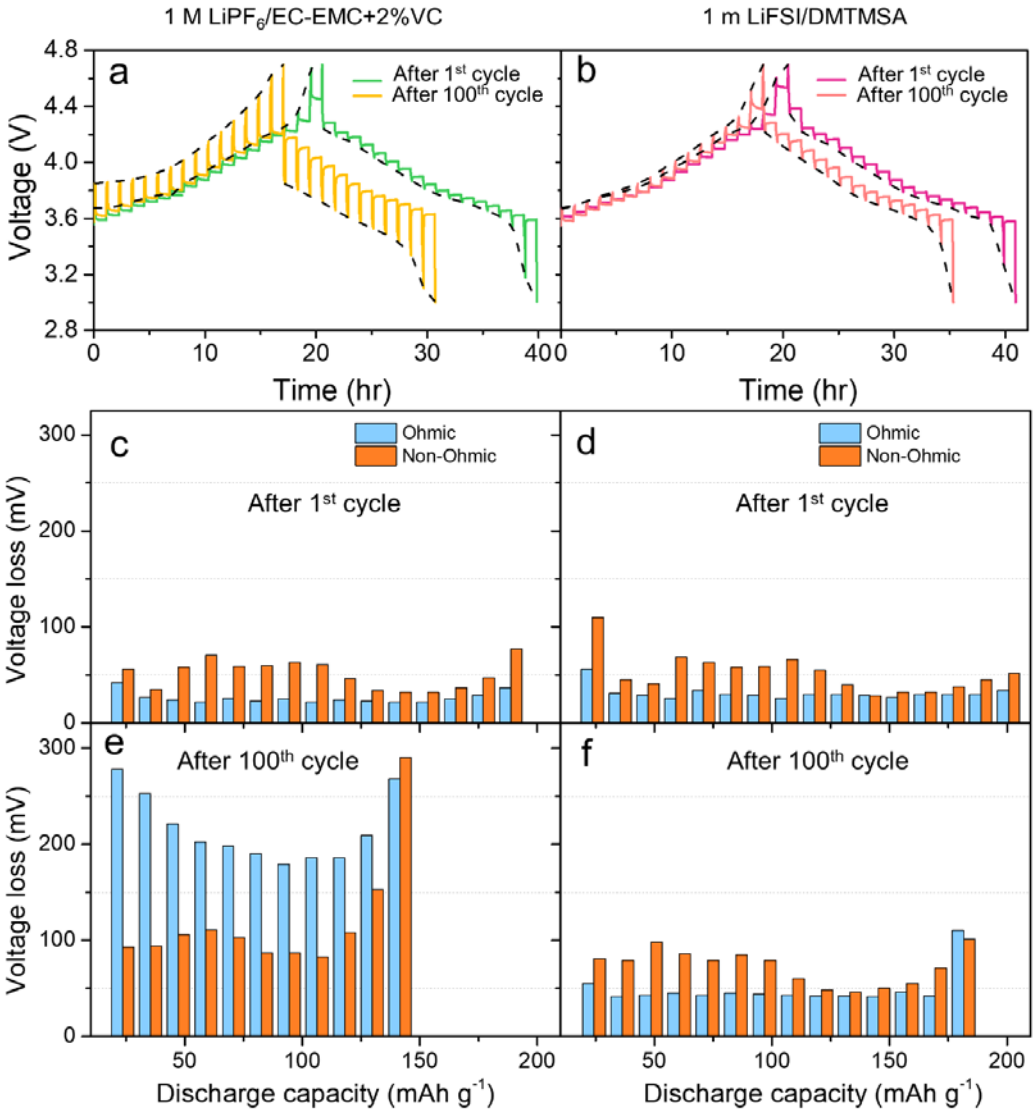

Supplementary Figure 7 Voltage-time profiles of GITT for the cells using the 1 M $LiPF_6$/EC-EMC+2% VC (a) and the 1 m LiFSI/DMTMSA (b) electrolytes measured after 1st and 100th cycles corresponding to Fig. 2a in the main text. The ohmic/non-ohmic voltage loss measured from (a) and (b) as a function of discharge capacity after 1st (c, d) and 100th (e, f) cycles in 1 M $LiPF_6$/EC-EMC+2% VC (c, e) and the 1 m LiFSI/DMTMSA (d, f) electrolytes.

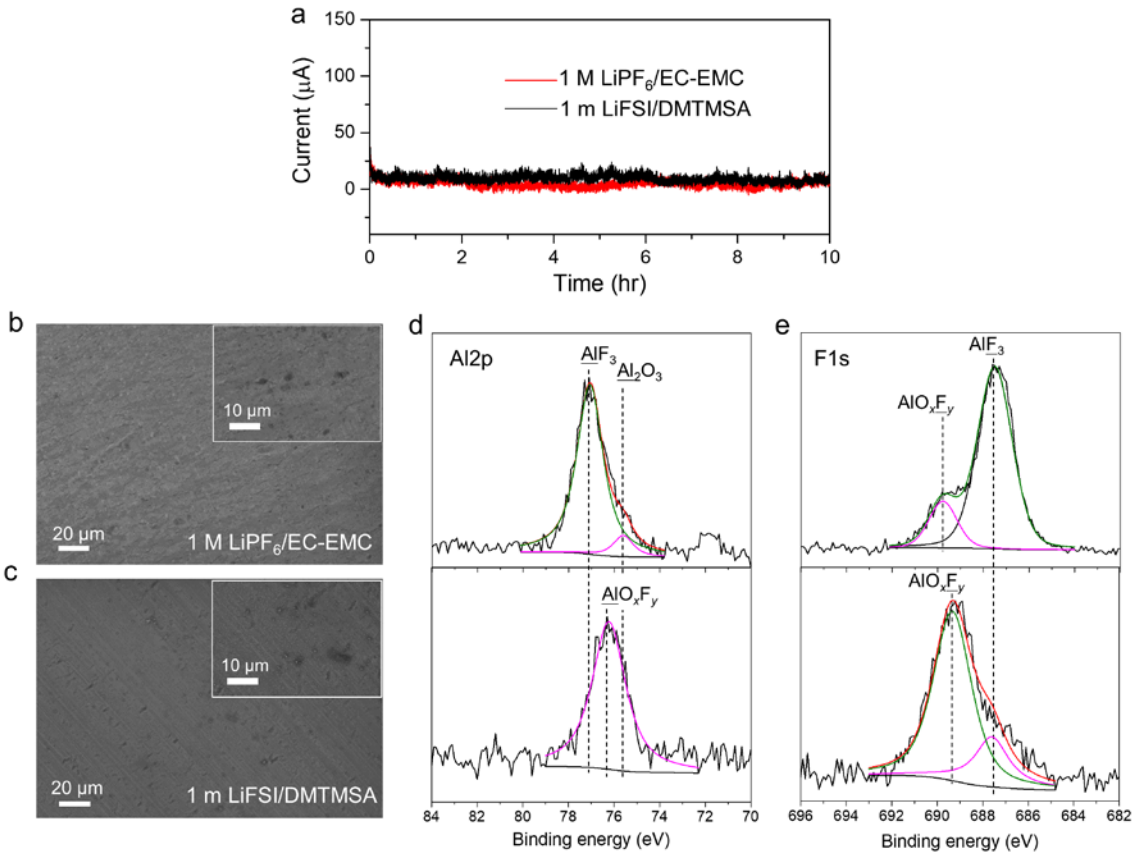

Supplementary Figure 8 Characterization of Al foils with 1 M $LiPF_6$/EC-EMC and 1 m LiFSI/DMTMSA electrolytes. (a) Leakage current as a functional of time during 4.7 V holding of Li||Al cells; (b, c) SEM images of the Al foils after 4.7 V holding experiments in (a). Surface chemistry of the Al foils in (b, c): Al 2*p* (d) and F 1*s* (e) signals from XPS measurements.

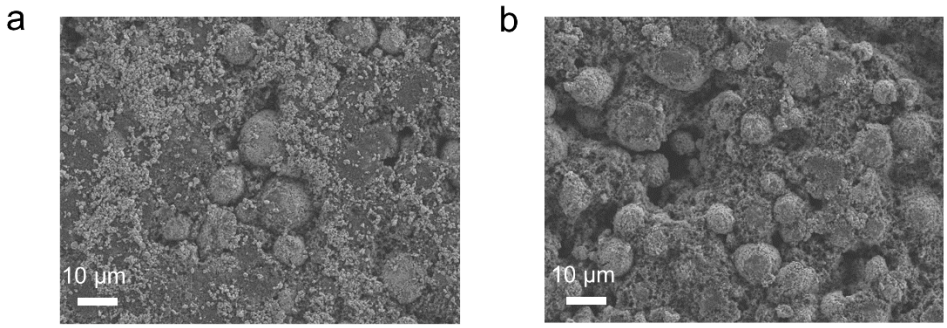

Supplementary Figure 9 SEM figures of the cathodes after floating test at 4.7 V for 20 hr in 1 M $LiPF_6$/EC-EMC+2% VC (a) and 1 m LiFSI/DMTMSA (b) electrolytes.

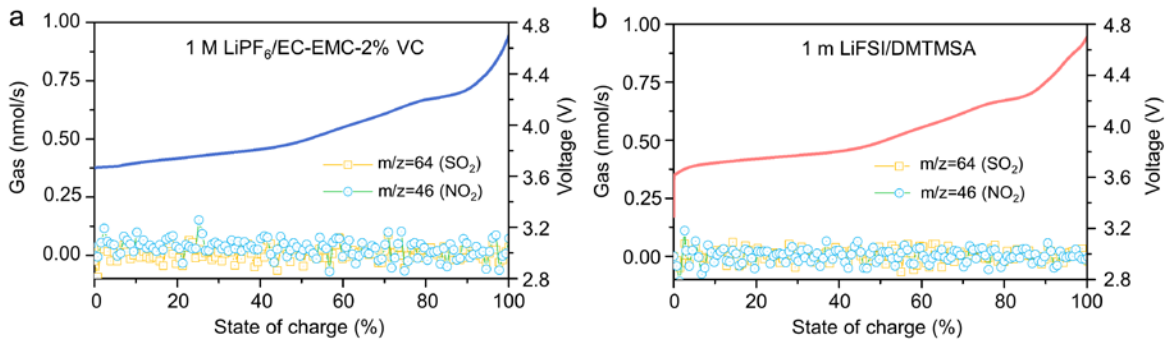

Supplementary Figure 10 The SO_2/NO_2 evolution during the 1st charge with 1 M $LiPF_6$/EC-EMC+2% VC (a) and 1 m LiFSI/DMTMSA (b) electrolytes.

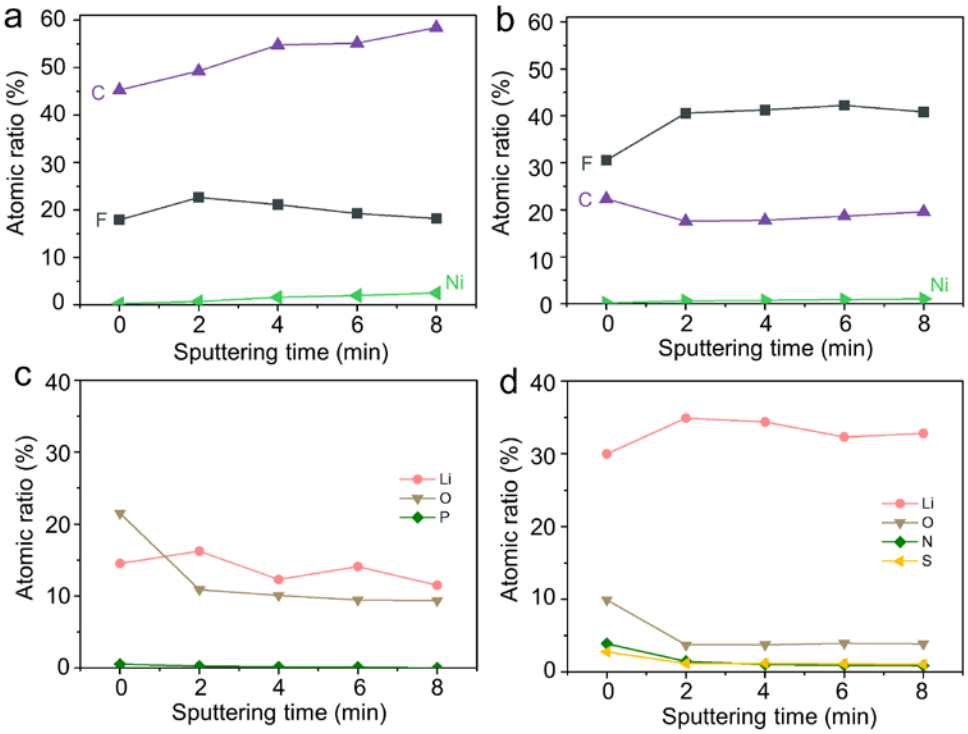

Supplementary Figure 11 Quantified C, F, Ni, Li, O, P, N, S atomic ratios of the CEI layers determined by XPS spectra for the NMC811 cathodes collected from cells with 1 M $LiPF_6$/EC-EMC+2% VC (a, c) and 1 m LiFSI/DMTMSA (b, d) electrolytes after 100 cycles.

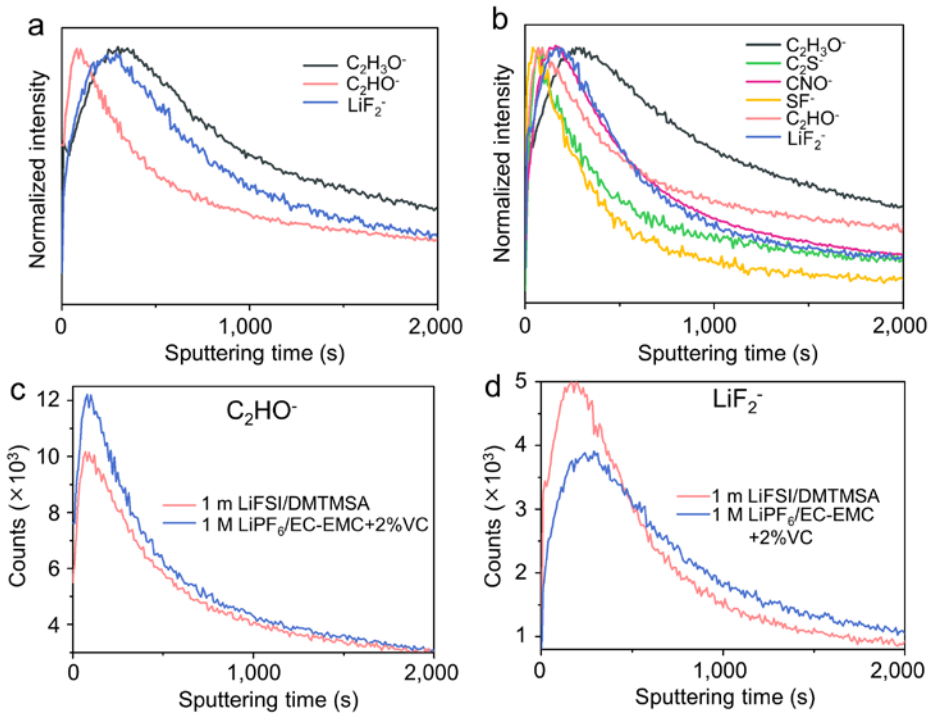

Supplementary Figure 12 Depth profiling from the TOF-SIMS results for the NMC811 cathodes after 100 cycles in 1 M $LiPF_6$/EC-EMC+2% VC (a) and 1 m LiFSI/DMTMSA (b) electrolytes where the peaks of different interested signals were normalized. The TOF-SIMS signals of C_2HO^- and LiF_2^- species obtained from the cycled cathodes in different electrolytes (before normalization) were compared in (c) and (d), respectively.

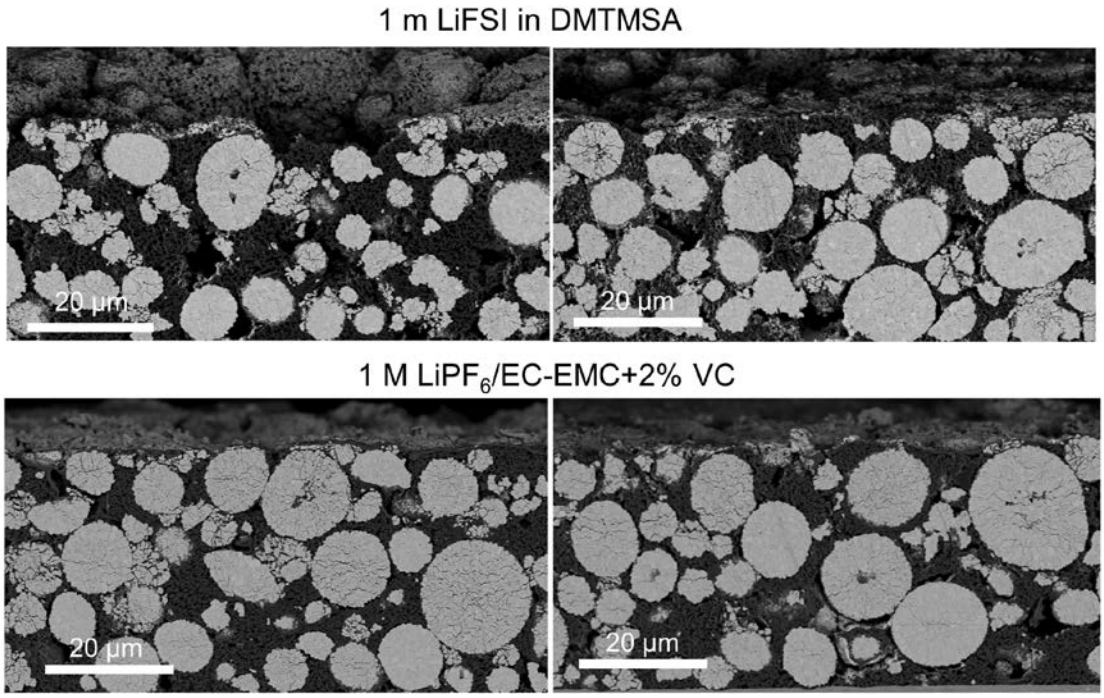

Supplementary Figure 13 SEM images of other cross-sections of the samples corresponding to Fig. 4 (a~d) in the main text

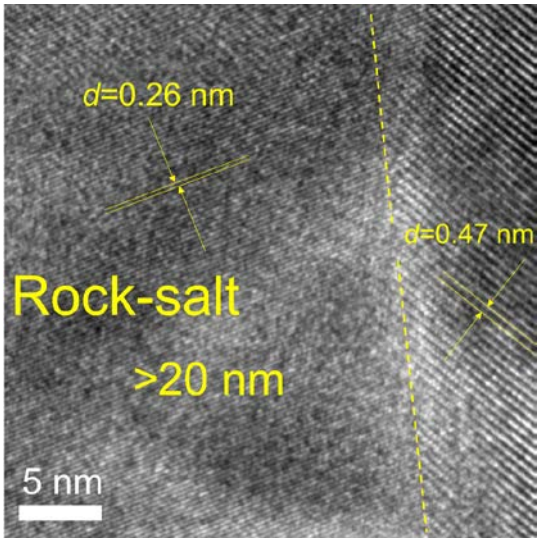

Supplementary Figure 14 HRTEM image of the NMC811 particle cycled in 1 M $LiPF_6$/EC-EMC-2% VC electrolyte for 100 cycles at 0.5 C.

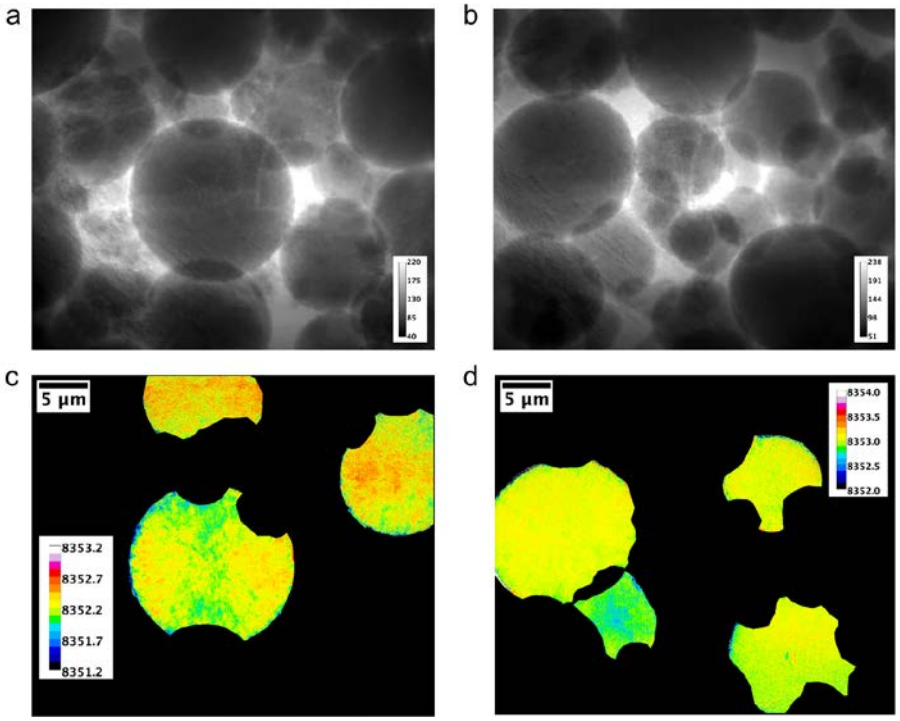

Supplementary Figure 15 Selection of the particles that are not overlapping with each other. (a, b) X-ray optical images of the electrode areas for the selection; (c, d) Selected particles. Cathodes were cycled in 1 M $LiPF_6$/EC-EMC+2% VC (a, b) and 1 m LiFSI/DMTMSA (b, d) for 100 cycles.

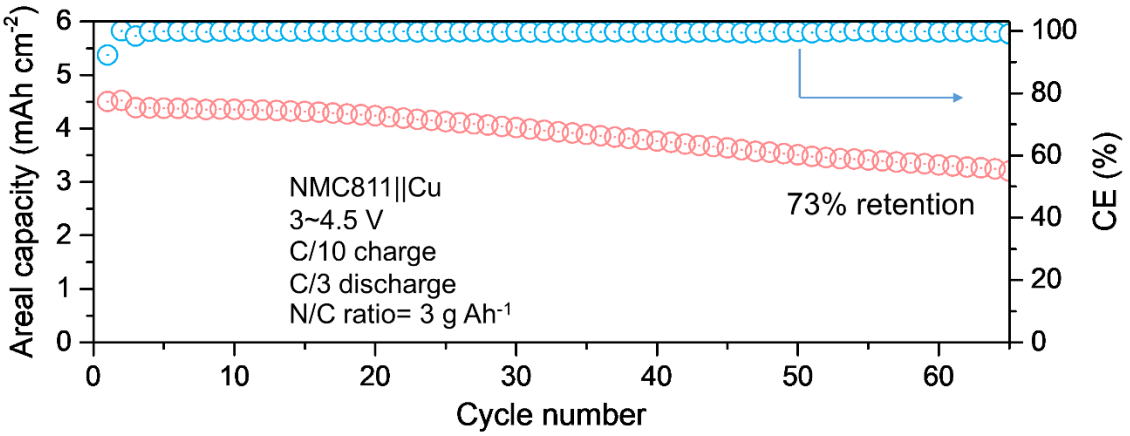

Supplementary Figure 16 Cycling performance of the anode-free NMC811||Cu cell in 1 m LiFSI/DMTMSA electrolyte with a bare Cu as the anode, 4.5 mAh cm^{-2} NMC811 cathode, and lean electrolyte (N/C=3 g Ah^{-1}) with C/10 charging and C/3 discharging (C/10 discharging for the initial 2 cycles) between 3~4.5 V at room temperature.

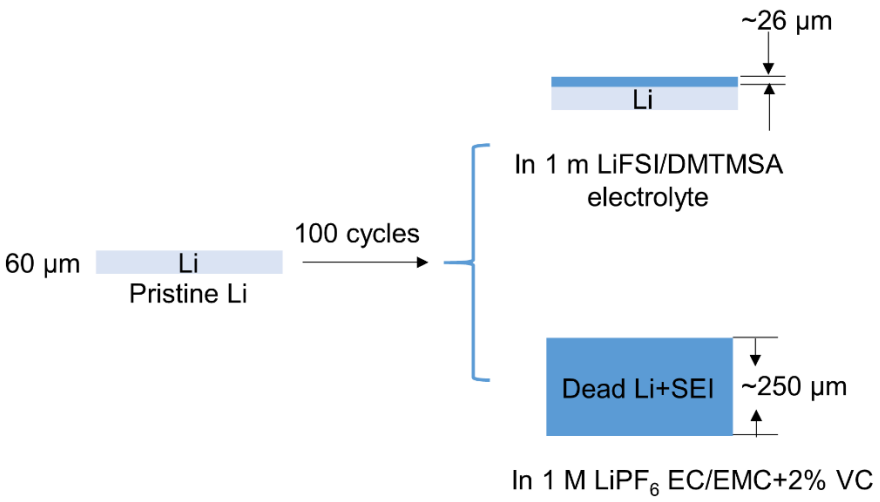

Supplementary Figure 17 Schematic figure illustrating the structure of the Li foil after 100 cycles in Li||NMC811 cells with different electrolytes (60 µm-thick Li foil was used). The thickness of the "garbage" layer cycled in the carbonate reference electrolyte was ~250 µm while that cycled in our sulfonamide-based electrolyte was only ~26 µm.

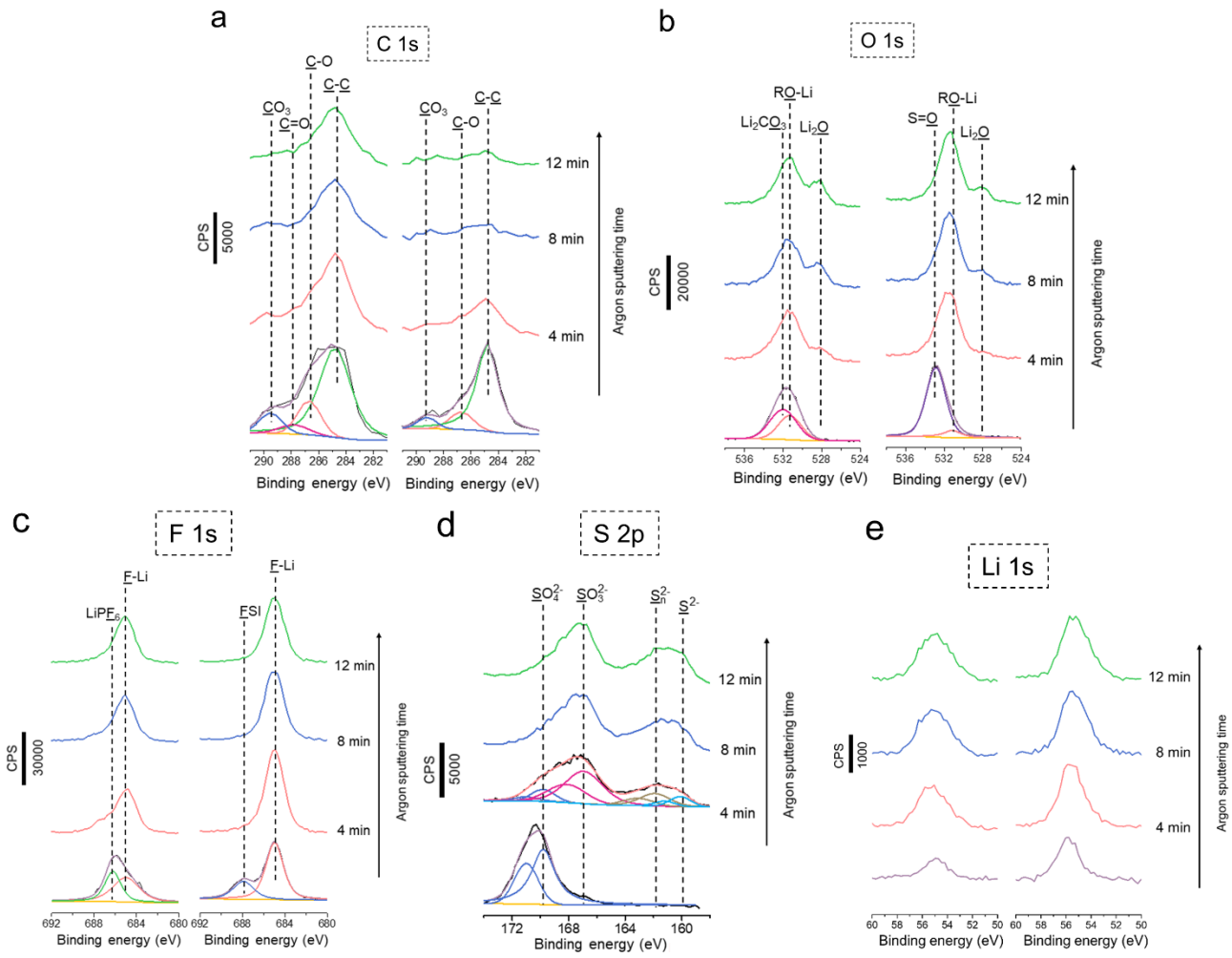

Supplementary Figure 18 Depth profiling XPS spectra for the lithium anode cycled in 1 M $LiPF_6$/EC-EMC+2% VC electrolyte (left side) and 1 m LiFSI/DMTMSA (right side) electrolytes (100 cycles at 0.5 C). (a), (b), (c) and (e) the C 1*s*, O 1*s*, F 1*s* and Li 1*s* spectra, respectively. (d) S 2*p* spectra of the Li anode cycled in 1 m LiFSI/DMTMSA electrolyte.

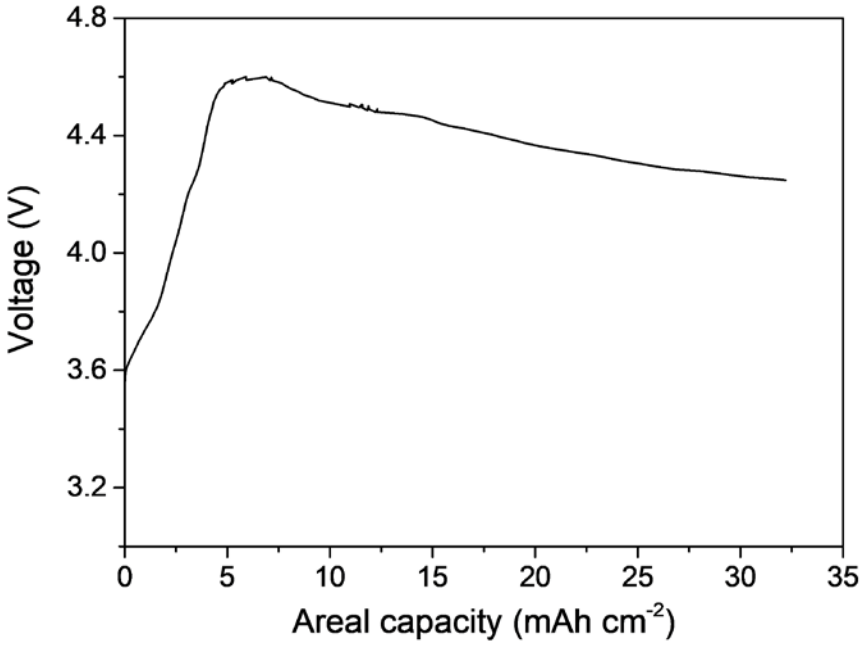

Supplementary Figure 19 The voltage profile of the 91st cycle in Fig. 7 of main text

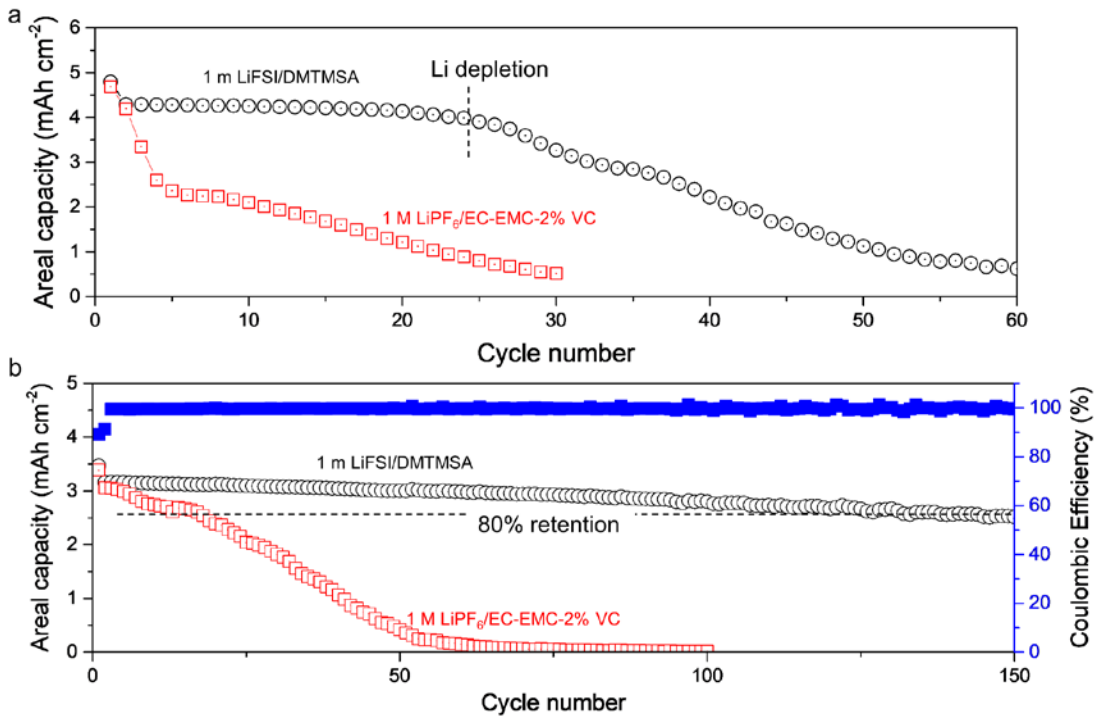

Supplementary Figure 20 Li||NMC811 cells cycled at higher charging/discharging rates within 3.0 V to 4.7 V in different electrolytes. (a) 0.5 C charging/1 C discharging. Mass loading~ 21.5 mg cm^{-2}, N/P ratio~ 0.4, E/C ratio~ 2.6 g Ah^{-1}; (b) 0.3 C charging/1 C discharging (0.1 C charging/discharging for the 1st cycle). Mass loading~ 15.3 mg cm^{-2}, N/P ratio~ 1, E/C ratio~ 3 g Ah^{-1}.

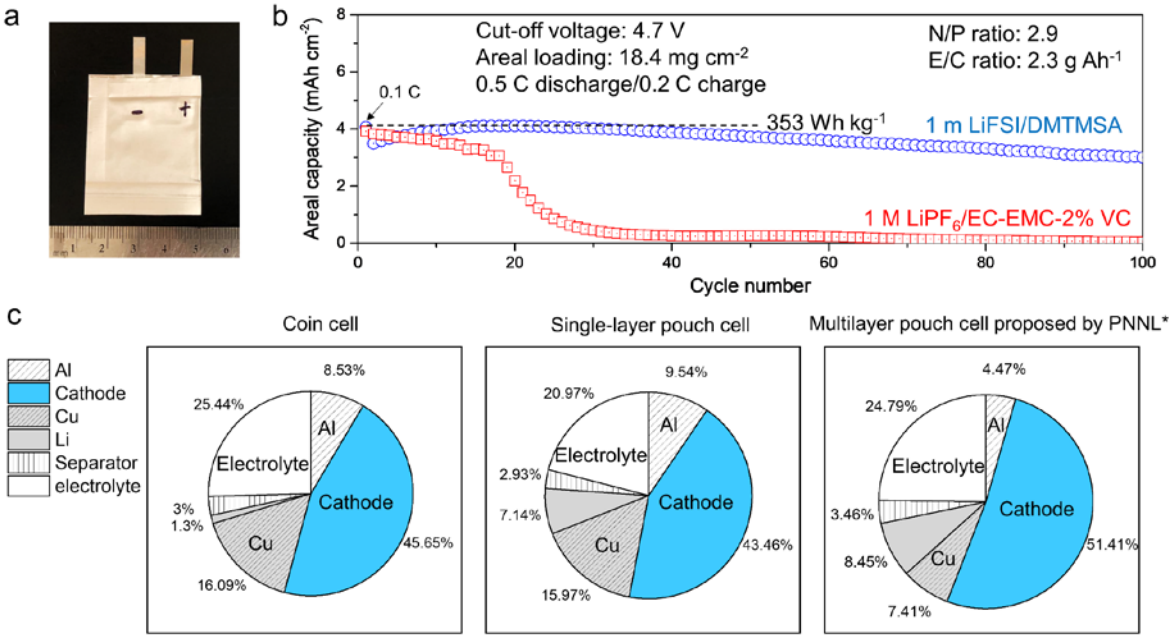

Supplementary Figure 21 Li||NMC811 pouch cell results with 1 m LiFSI/DMTMSA and 1 M $LiPF_6$/EC-EMC-2%VC electrolytes. (a) Photo of the assembled pouch cell. (b) Cycling performance of pouch cells using different electrolytes with 0.5 C/0.2 C discharge/charge. Upper cut-off voltage is 4.7 V vs. Li^+/Li. Active material loading is 18.4 mg cm^{-2}. E/C and N/P ratios are 2.3 g Ah^{-1} and 2.9, respectively. Cathode loading: 18.4 mg cm^{-2}. E/C ratio: 2.3 g Ah^{-1}. N/P ratio: 2.9. (c) Weight ratios of cell components in jellyrolls of coin cell, and single-layer and multilayer pouch cells.

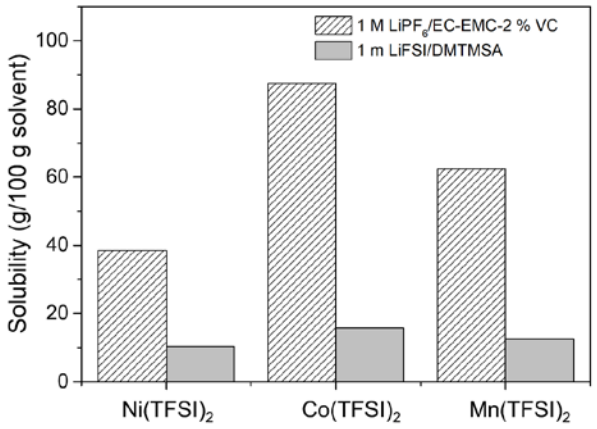

Supplementary Figure 22 The solubilities of $Ni(TFSI)_2$, $Co(TFSI)_2$ and $Mn(TFSI)_2$ in 1 m LiFSI/DMTMSA and 1 M $LiPF_6$/EC-EMC-2% VC

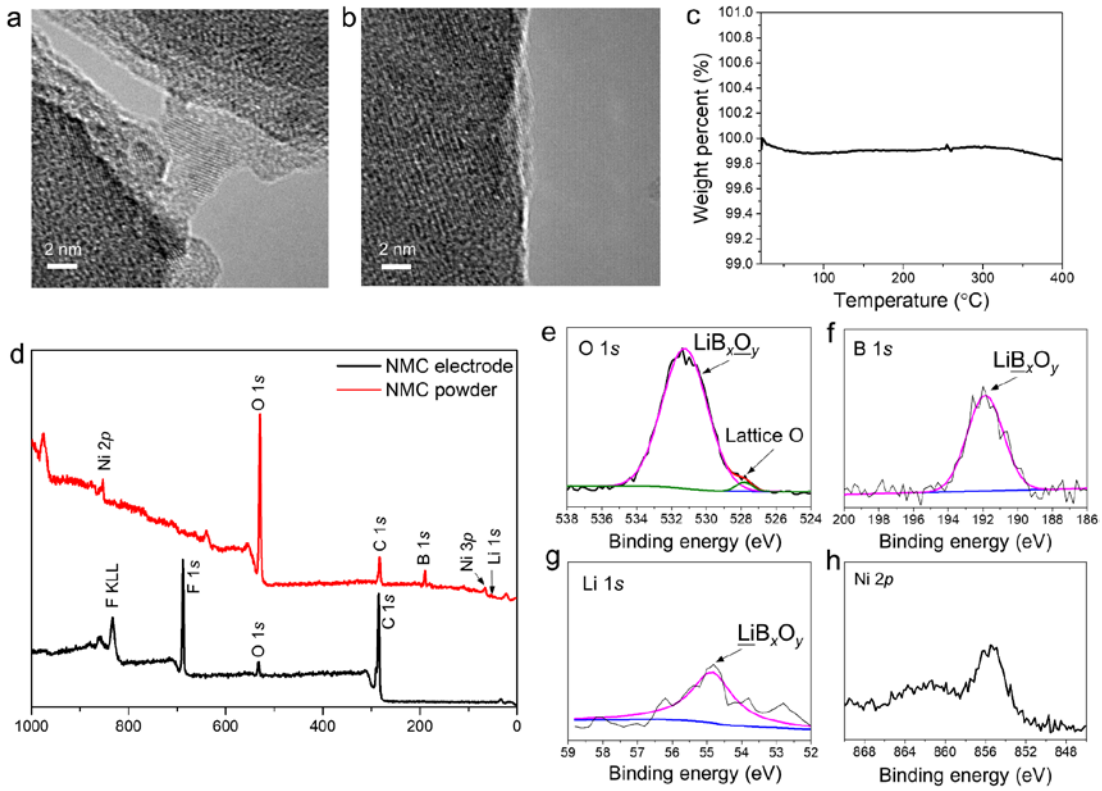

Supplementary Figure 23 Characterization on the surface coating claimed by the vendor. (a, b) HRTEM images and (c) thermal gravimetric analysis (TGA) of the pristine NMC811 powder; (d) XPS survey of the pristine NMC811 powder and electrode; (e~h) XPS spectra of O 1*s*, B 1*s*, Li 1*s* and Ni 2*p* of the pristine NMC811 powder

We further conducted characterizations on the pristine NMC811 powders and electrodes. In a local region of the particle surface, a thin (~2 nm) coating layer was found as shown by the HRTEM image in (a). Yet the coating is not very uniform, as it is absence in another local region in (b). We also conducted thermal gravimetric analysis on the pristine powder to confirm that the coating layer is not a polymer due to lack of mass loss upon heating up to 400 ^{o}C (c). Lastly, we conducted XPS measurement on the pristine NCM811 powders and electrodes. Boron is noted from the XPS survey (d) on the pristine powders, but it cannot be detected on the NMC811 electrodes probably due to of the coverage of PVDF binder and conductive carbon. The XPS spectra of O 1*s*, B 1*s* and Li 1*s* (e, f, g) indicate that the coating layer could be LiB_xO_y.

Supplementary Table 1. Comparison of our work with recent electrolyte works on Li(or graphite)||NMC batteries

Composition	Cathode side				Cyclability	High salt concentration	Li-Anode	Cell parameters		
	Cathode	Cut-off voltage	Specific capacity	CE			CE (Li-Cu)	High cathode loading	Low N/C ratio	Low N/P ratio
1 m LiFSI in DMTMSA (our work)	**NMC811**	**4.7 V**	**231 mAh g^{-1}**	**99.65%**	**88.1% (100 cycles)**	**NO**	**~99%**	**~21.5 mg cm^{-2}**	**2.62 g Ah^{-1}**	**0.39**
10 M LiFSI in DMC[1]	NMC622	4.6 V	~225 mAh g^{-1}	>99.6%	86% (100 cycles)	YES	>99%	NO	NO	NO
1 M $LiPF_6$ in FEC/FEMC/HFE[2]	NMC811	4.4 V	~200 mAh g^{-1}	~99.93%	90% (450 cycles)	NO	>99%	NO	NO	1
0.6 M LiTFSI+0.4 M LiBOB+0.05 M $LiPF_6$[3]	$LiNi_{0.76}Mn_{0.14}Co_{0.10}O_2$	4.5 V	~220 mAh g^{-1}	99.5%	90% (200 cycles)	NO	—	NO	NO	NO
3.1 M $LiPF_6$ in EC/EMC[4]	NMC811	4.6 V	~220 mAh g^{-1}	—	77% (500 cycles)	YES	—	NO	NO	NO
4.6 m LiFSI+ 2.3 m LiTFSI in DME[5]	NMC622	4.4 V	~165 mAh g^{-1}	—	88% (300 cycles)	YES	98.2%	NO	NO	NO
1.2 m LiFSI in DMC-BTFE[6]	NMC333	4.3 V	~162 mAh g^{-1}	~99.7%	80% (700 cycles)	NO	99.3%	NO	NO	NO
2 M LiTFSI + 2 M LiDFOB in DME[7]	NMC333	4.3 V	~163 mAh g^{-1}	—	97.1% (500 cycles)	YES	98.4%	NO	NO	NO
LiFSI-1.2DME-3TTE[8]	NMC811	4.5 V	~223 mAh g^{-1}	99.77%	82% (250 cycles)	NO	99.1%	> 20 mg cm^{-2}	3 g Ah^{-1}	2.38
1M LiFSI-DME-TFEO[9]	NMC811	4.4 V	~210 mAh g^{-1}	99.7%	80% (300 cycles)	NO	99.5%	NO	NO	NO
1 M LiFSI/FDMB[10]	NMC811	4.4 V	—	—	~68% (100 cycles)	NO	~99.5%	3-4 mAh cm^{-2}	~1 g Ah^{-1}	0
$LiPF_6$/EC-DEC-$LiNO_3$-$Sn(OTf)_2$[11]	NMC811	4.3 V	~200 mAh g^{-1}	—	89.6% (130 cycles)	NO	98.4%	16.7 mg cm^{-2}	10 µL mAh^{-1}	2.64
	NMC532	4.5 V	~205 mAh g^{-1}	—	86.2% (120 cycles)	NO		20 mg cm^{-2}	40 µL	2.28
1 M $LiPF_6$/FEC-EMC-$LiNO_3$-TPFPB[12]	NMC811	4.5 V	~232 mAh g^{-1}	—	75.4% (100 cycles)	NO	98.5%	4 mAh cm^{-2}	~3.4 g Ah^{-1}	2.5

1.2 M LiFSI/TEP-BTFE[13]	NMC622	4.4 V	185 mAh g^{-1}	—	86% (200 cycles)	NO	—	20.5 mg cm^{-2}	3.0 g Ah^{-1}	2.6
1 M LiDFOB+0.2 M $LiBF_4$/FEC-DEC (1:2 v)[14]	NMC532	4.5 V	~160 mAh g^{-1}	—	80% (90 cycles)	NO	—	2.4 mAh cm^{-2}	~1.8 g Ah^{-1}	0
1M $LiBF_4$ in FEC:SN[15]	NMC532	4.7 V	~185 mAh g^{-1}	—	73.6% (100 cycles)	NO	—	2.5 mg cm^{-2}	NO	NO
1 M $LiPF_6$/EC-DEC-EMC-10 wt% FEC[16]	NMC622	4.6 V	~199 mAh g^{-1}	—	87.3% (100 cycles)	NO	—	—	—	—
8.67 m $LiBF_4$/DMC[17]	NMC532	4.6 V	200 mAh g^{-1}	~99%	92.2% (50 cycles)	YES	—	—	NO	NO
1 M $LiPF_6$/EC-DEC-DMC-3 wt% TMB[18]	NMC333	4.5 V	~160 mAh g^{-1}	—	99% (300 cycles)	NO	—	1.6 mg cm^{-2}	NO	NO
1 M $LiBF_4$/EC-DMC(1/1 wt)[19]	NMC333	4.6 V	~164 mAh g^{-1}	—	96.4% (50 cycles)	NO	—	1.8 mg cm^{-2}	NO	NO

Composition	**Cathode side**				**Cyclability**	**High salt concentration**	**Graphite (Gr) Anode**	**Cathode loading**	**Cell configuration**
	Cathode	**Cut-off voltage**	**Specific capacity**	**CE**					
1 M LiFSI-0.5 M $LiPF_6$/EMC + 3% VC[20]	$LiNi_{0.94}Co_{0.06}O_2$	4.2 V	~222 mAh g^{-1}	—	81% (1000 cycles)	NO	Gr	11.5 mg cm^{-2}	Pouch cell
1 M $LiPF_6$/FEC-EMC (5:95)[21]	NMC442	4.4 V	—	—	93% (500 cycles)	NO	Gr	—	Pouch cell
	NMC532	4.4 V	—	—	85% (~3000 cycles)	NO	Gr		
1.0 M $LiPF_6$/FEC-FEMC (1/9, v/v)[22]	NMC532	4.7 V	~190 mAh g^{-1}	~99%	81% (200 cycles)	NO	Gr	2 mAh cm^{-2}	Coin cell
1 M $LiPF_6$ FEC/HFDEC[23]	NMC532	4.6 V	~220 mAh g^{-1}	—	82% (100 cycles)	NO	Gr	9.15 mg cm^{-2}	Coin cell
1.0 M $LiPF_6$/EMC-VC-1% PPF[24]	NMC442	4.4 V	—	—	80% (350 cycles)	NO	Gr	—	Pouch cell

Supplementary Table 2 Li^+ conductivity in different electrolytes

	Li^+ conductivity (mS cm^{-1})
1 M $LiPF_6$/EC-EMC-2% VC	9.91
1 M $LiPF_6$/EC-EMC	9.72
1 m LiFSI/DMTMSA	1.37
0.5 m LiFSI/DMTMSA	1.09
1.5 m LiFSI/DMTMSA	1.26

Supplementary Table 3 Basic properties of carbonate and sulfonamide-based electrolytes

	Li^+ conductivity (mS cm^{-1})	Li^+ transference number	Viscosity (mPa s)	Water content (ppm)	Density (g cm^{-3})	Contact angle (°)
1 M $LiPF_6$/ EC-EMC-2% VC	9.91	0.51	3.8	45.0	1.2	47.0
1 m LiFSI/ DMTMSA	1.37	0.62	4.4	42.5	1.4	23.4

Supplementary Table 4 Parameters used for calculating the specific energy of the single-layer pouch cell

	Weight (mg)
Cathode	109.9
Anode	47.9
Separator	6.1
Electrolyte	43.5
Total weight (mg)	207.4

Supplementary Table 5 Parameters used for estimating the specific energy in multilayer pouch cell configuration [*]

	Parameters	Areal weight (mg cm^{-2})	Layers	Area (cm^2)	Total weight (mg)
Cu	6 μm	5.37	10	31.5	1691.6
Al	12 μm	3.24	10	31.5	1020.6
NMC811 cathode	~96 μm	19.6	19	31.5	11730.6
Li	60 μm	3.22	19	31.5	1927.2
Separator	16 μm	1.32	19	31.5	790.0
Electrolyte	E/C ratio=2.3 g Ah^{-1}				5655.6

[*]The parameters of Cu&Al current collectors and separator are from *Nature Energy* **4**, 180-186 (2019). Other parameters are the same as those for single-layer pouch cell in Table S4.

Supplementary Table 6 Costs of the chemicals used for DMTMSA solvent synthesis

	Role	Grade	Price	Vendor
Dimethylamine	Raw material	≥99%	$303/kg	Sigma Aldrich
Trifluoromethanesulfonyl chloride	Raw material	≥99.0%	$4935/kg	Fisher Scientific
Dichloromethane	Solvent	≥99.8%	$40.5/L	Sigma Aldrich
Tetrahydrofuran	Solvent	≥99.0%	$40.3/L	Sigma Aldrich
Triethylamine	Removing byproduct HCl	For synthesis	$14.7/kg	Sigma Aldrich

$ is US dollar

Supplementary Note

Further explanation about the fitting method of the TXM data:

Empirically it is known that there are correlations between formal charge state and edge shifts in many systems. As stated in the XAS tutorials[25, 26] and review articles[27], using whiteline shift to qualitatively indicate the concerned element valence state is a common practice. In conventional bulk XAS cases, it is rare only to use this kind of qualitative analysis approach since the data qualities in these cases are good enough, so it is feasible and doable to fit a limited number of spectra in individual study cases. However, it is different in TXM XANES cases in which the signal at each pixel is from an area only at 10^3 nm^2 scale. As a comparison, the signal in a conventional bulk XAS spectrum is from an area typically larger than 10^{12} nm^2 area. Besides, the number of spectra in a TXM XANES case is in the range from 1 million to 1 billion. It is practically impossible to perform quantitative XANES fittings as those are used in conventional XAS cases. For such reasons, using whiteline shift as the indications of concerned element valence state changes is typically used in TXM XANES analysis[28-31].

Supplementary References

1. Fan X., *et al.* Highly fluorinated interphases enable high-voltage Li-metal batteries. *Chem* **4**, 174-185 (2018).
2. Fan X., *et al.* Non-flammable electrolyte enables Li-metal batteries with aggressive cathode chemistries. *Nat. Nanotechnol.* **13**, 715-722 (2018).
3. Zhao W., *et al.* High voltage operation of Ni-rich NMC cathodes enabled by stable electrode/electrolyte interphases. *Adv. Energy Mater.* **8**, 1800297 (2018).
4. Tatara R., *et al.* Enhanced cycling performance of Ni-rich positive electrodes (NMC) in Li-Ion batteries by reducing electrolyte free-solvent activity. *ACS Appl. Mater. Interfaces* **11**, 34973-34988 (2019).
5. Alvarado J., *et al.* Bisalt ether electrolytes: a pathway towards lithium metal batteries with Ni-rich cathodes. *Energy Environ. Sci.* **12**, 780-794 (2019).
6. Chen S., *et al.* High-voltage lithium-metal batteries enabled by localized high-concentration electrolytes. *Adv. Mater.* **30**, 1706102 (2018).
7. Jiao S., *et al.* Stable cycling of high-voltage lithium metal batteries in ether electrolytes. *Nat. Energy* **3**, 739-746 (2018).
8. Ren X., *et al.* Enabling high-voltage lithium-metal batteries under practical conditions. *Joule* **3**, 1662-1676 (2019).
9. Cao X., *et al.* Monolithic solid-electrolyte interphases formed in fluorinated orthoformate-based electrolytes minimize Li depletion and pulverization. *Nat. Energy* **4**, 796-805 (2019).
10. Yu Z., *et al.* Molecular design for electrolyte solvents enabling energy-dense and long-cycling lithium metal batteries. *Nat. Energy* **5**, 526-533 (2020).
11. Zhang W., *et al.* Colossal granular lithium deposits enabled by the grain-coarsening effect for high-efficiency lithium metal full batteries. *Adv Mater* **32**, 2001740 (2020).
12. Li S., *et al.* Synergistic dual-additives electrolyte enables practical lithium metal batteries. *Angew. Chem. Int. Ed.* **59**, 14935-14941 (2020).
13. Niu C., *et al.* High-energy lithium metal pouch cells with limited anode swelling and long stable cycles. *Nat. Energy* **4**, 551-559 (2019).
14. Weber R., *et al.* Long cycle life and dendrite-free lithium morphology in anode-free lithium pouch cells enabled by a dual-salt liquid electrolyte. *Nat. Energy* **4**, 683-689 (2019).
15. Zhang Q., *et al.* Enhancing the high voltage interface compatibility of $LiNi_{0.5}Co_{0.2}Mn_{0.3}O_2$ in the succinonitrile-based electrolyte. *Electrochim. Acta* **298**, 818-826 (2019).
16. Liu L., *et al.* Fluoroethylene carbonate as an electrolyte additive for improving interfacial stability of high-voltage $LiNi_{0.6}Co_{0.2}Mn_{0.2}O_2$ cathode. *Ionics* **25**, 1035-1043 (2018).

17. Doi T., *et al.* Fluoroalkyl ether-diluted dimethyl carbonate-based electrolyte solutions for high-voltage operation of $LiNi_{0.5}Co_{0.2}Mn_{0.3}O_2$ electrodes in lithium ion batteries. *Sustainable Energy & Fuels* **2**, 1197-1205 (2018).
18. Yu Q., *et al.* Enhanced high voltage performances of layered lithium nickel cobalt manganese oxide cathode by using trimethylboroxine as electrolyte additive. *Electrochim. Acta* **176**, 919-925 (2015).
19. Gallus D.R., *et al.* The influence of different conducting salts on the metal dissolution and capacity fading of NCM cathode material. *Electrochim. Acta* **134**, 393-398 (2014).
20. Li W., Dolocan A., Li J., Xie Q. & Manthiram A. Ethylene carbonate-free electrolytes for high-nickel layered oxide cathodes in lithium-ion batteries. *Adv. Energy Mater.* **9**, 1901152 (2019).
21. Logan E.R., *et al.* A study of the transport properties of ethylene carbonate-free Li electrolytes. *J. Electrochem. Soc.* **165**, A705-A716 (2018).
22. Im J., Lee J., Ryou M.-H., Lee Y.M. & Cho K.Y. Fluorinated carbonate-based electrolyte for high-voltage $Li(Ni_{0.5}Mn_{0.3}Co_{0.2})O_2$/graphite lithium-ion battery. *J. Electrochem. Soc.* **164**, A6381-A6385 (2017).
23. He M., *et al.* High voltage $LiNi_{0.5}Mn_{0.3}Co_{0.2}O_2$/graphite cell cycled at 4.6 V with a FEC/HFDEC-based electrolyte. *Adv. Energy Mater.* **7**, 1700109 (2017).
24. Petibon R., *et al.* Electrolyte system for high voltage Li-ion cells. *J. Electrochem. Soc.* **163**, A2571-A2578 (2016).
25. Bunker G. Interpreting XANES (http://gbxafs.iit.edu/training/XANES_intro.pdf)
26. Newville M Fundamentals of XAFS (https://docs.xrayabsorption.org/tutorials/XAFS_ Fundamentals.pdf)
27. Henderson G S, De Groot F M F and Moulton B J A. X-ray absorption near-edge structure (XANES) spectroscopy. *Reviews in Mineralogy and Geochemistry*, 2014, 78, 75-138.
28. Mu L, Yuan Q, Tian C, Wei C, Zhang K, Liu J, Pianetta P, Doeff M M, Liu Y and Lin F. Propagation topography of redox phase transformations in heterogeneous layered oxide cathode materials. *Nature Communications*, 2018, 9, 2810.
29. Kuppan S, Xu Y, Liu Y and Chen G. Phase transformation mechanism in lithium manganese nickel oxide revealed by single-crystal hard X-ray microscopy. *Nature Communications*, 2017, 8, 1-10.
30. Boesenberg U, Meirer F, Liu Y, Shukla A K, Dell'anna R, Tyliszczak T, Chen G, Andrews J C, Richardson T J, Kostecki R and Cabana J. Mesoscale phase distribution in single particles of $LiFePO_4$ following lithium deintercalation. *Chemistry of Materials*, 2013, 25(9), 1664-1672.
31. Wolf M, May B M and Cabana J. Visualization of electrochemical reactions in battery materials with X-ray microscopy and mapping. *Chemistry of Materials*, 2017, 29, 3347-62.